ELSEVIER

Journal of Fluids and Structures 25 (2009) 1136–1157

JOURNAL OF FLUIDS AND STRUCTURES

www.elsevier.com/locate/jfs

Linear stability analysis of coupled parallel flexible plates in an axial flow

S. Michelin[a,b,*], S.G. Llewellyn Smith[a]

[a]*Department of Mechanical and Aerospace Engineering, Jacobs School of Engineering, UCSD, 9500 Gilman Drive, La Jolla, CA 92093-0411, USA*

[b]*Ecole Nationale Supérieure des Mines de Paris, 60–62 Boulevard Saint Michel, 75272 Paris cedex 06, France*

Received 22 January 2009; accepted 13 June 2009
Available online 19 August 2009

Abstract

We study here the linear stability of N identical flexible plates with clamped–free boundary conditions forced by a uniform parallel flow. Flow viscosity and elastic damping are neglected, and the flow around the plates is assumed potential. The shedding of vorticity from the plates' trailing edges is accounted for by introducing a force-free wake behind each plate. A Galerkin method is used to compute the eigenmodes of the system. We are interested in the effects of the number of plates and their relative distance on the stability property of the state of rest, as well as in the nature and structure of the coupled states. Detailed results are presented for the cases $N = 2$, $N = 3$ and $N \gg 1$.
© 2009 Elsevier Ltd. All rights reserved.

PACS: 46.70.De; 46.40.−f; 47.20.Cq

Keywords: Flow-induced vibration; Flutter instability; Plate-assemblies

1. Introduction

The flapping motion of flexible plates or flags placed in a parallel imposed flow has been the subject of a large number of both experimental (Zhang et al., 2000; Shelley et al., 2005) and numerical studies (Connell and Yue, 2007; Zhu and Peskin, 2002). The flapping motion results from the fluttering instability of the plate's straight position under the competing effects of solid inertia, aerodynamic pressure forcing and solid flexural rigidity. In that regard, the nature of the instability is similar to that of flow-conveying pipes (Païdoussis, 1998). Beyond the fundamental interest of this instability and the resulting flapping motions, this mechanism is at the origin of the flapping of flags in the wind and is also of interest for engineering (Watanabe et al., 2002) and biomedical applications (Huang, 1995; Balint and Lucey, 2005). Hydroelastic instabilities of parallel-plate assemblies are also important in the study of industrial cooling systems, as found in some nuclear reactors (Miller, 1960; Kim and Davis, 1995; Guo and Païdoussis, 2000a).

Several models have been proposed to understand the instability threshold in the case of a single elastic plate. Shelley et al. (2005) considered the one-dimensional linear stability of a flag of infinite span and length under parallel flow

*Corresponding author at: Department of Mechanical and Aerospace Engineering, Jacobs School of Engineering, UCSD, 9500 Gilman Drive, La Jolla, CA 92093-0411, USA.
E-mail address: smichelin@ucsd.edu (S. Michelin).

0889-9746/$ - see front matter © 2009 Elsevier Ltd. All rights reserved.
doi:10.1016/j.jfluidstructs.2009.06.002

forcing. Lemaitre et al. (2005) used a slender-body approximation to study the linear stability of long elastic ribbons. Kornecki et al. (1976) studied the linear stability of a finite-length cantilevered plate of infinite span, using a representation of the vortical wake as a vortex sheet (Theodorsen, 1935; Bisplinghoff et al., 1955), and Argentina and Mahadevan (2005) used a similar approach to study the influence of in-plane tension and finite span on the stability threshold. Guo and Païdoussis (2000b) considered the stability of a finite-length two-dimensional plate in a channel with various boundary conditions, using a simpler representation of the wake. Eloy et al. (2007) used the same approach to investigate the influence of three-dimensional effects on the stability of a finite-length cantilevered plate.

In the case of multiple parallel elastic plates, the imposed flow acts both as a forcing and a coupling mechanism between the motion of the plates. When the distance between the plates is of the order of or less than their length, it is expected that their dynamics will be strongly coupled. Zhang et al. (2000) generalized their soap-film experiment to two parallel filaments and showed that the filaments' dynamics became coupled and that, depending on their relative distance, in-phase and out-of-phase modes could be observed (Fig. 1). This observation was confirmed by Jia et al. (2007) who also considered filaments of various lengths. Depending on the length of the filaments, they observed either a transition from out-of-phase to in-phase flapping when bringing the filaments close together, or a persistence of the out-of-phase mode even at small separation. These results suggest that the nature of the observed regime is strongly dependent on more than just the relative distance between the different plates or filaments. Numerical simulations (Zhu and Peskin, 2003; Farnell et al., 2004; Huang et al., 2007; Michelin and Llewellyn Smith, 2009) have also reported the existence of these two classes of regimes. Tang and Païdoussis (2009) presented a numerical study of the stability criteria for the in-phase and out-of-phase modes. More recently, Schouveiler and Eloy (2009, private communication) considered three and more coupled plates in a wind-tunnel experiment and observed various mode structures (Fig. 1). In particular, in the symmetric mode, the middle plate was observed to remain still. Guo and Païdoussis (2000a) studied the linear stability of an infinite number of parallel plates of finite aspect ratio, clamped on their side edges and free at the leading and trailing edges. They however focused only on one particular type of modes (the out-of-phase mode, where the motions of two consecutive plates are always opposite), using the resulting symmetries to significantly reduce the complexity of the system.

The purpose of the present study is to propose a linear stability analysis of N coupled flexible plates of infinite span, clamped at their leading edge in a uniform imposed flow. We investigate the existence and nature of coupled modes, that were previously observed experimentally and numerically (Zhang et al., 2000; Zhu and Peskin, 2003; Jia et al., 2007), as well as the influence of the plates' separation on the stability of the trivial state of rest and the structure of the linearly dominant flapping modes. In Section 2, the double-wake method used in Guo and Païdoussis (2000b) and Eloy et al. (2007) for a single plate is extended to the case of an arbitrary number of equidistant parallel plates. In Sections 3 and 4, results on the linear stability of respectively two and three plates and the structure of the most unstable modes are discussed. Section 5 proposes an overview of expected results at larger N as well as a discussion of the influence of N on

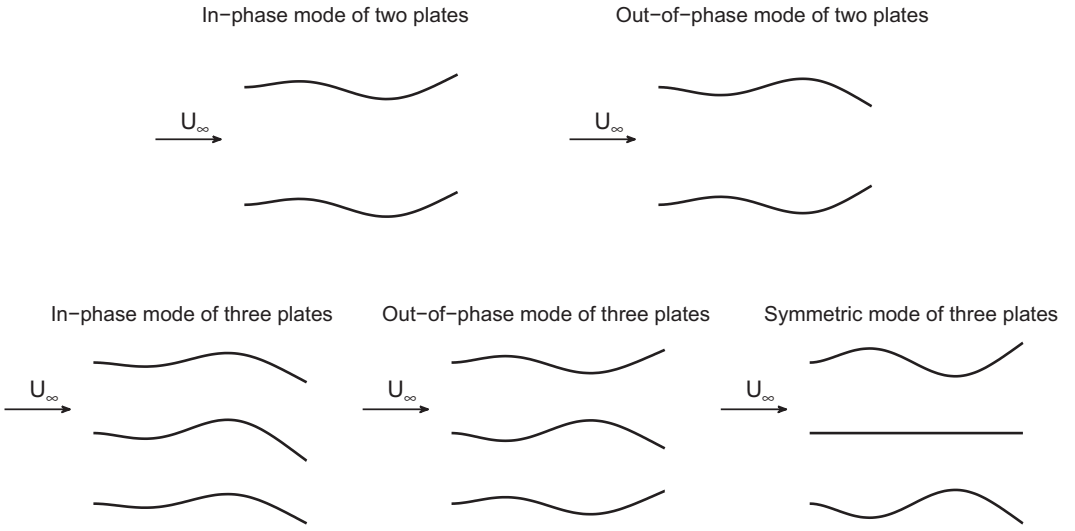

Fig. 1. (Top) Sketch of the in-phase and out-of-phase modes observed experimentally for two plates (Zhang et al., 2000; Jia et al., 2007). (Bottom) Sketch of the in-phase, out-of-phase and symmetric modes observed experimentally for three plates (Schouveiler and Eloy, 2009, private communication).

the critical stability curve for a fixed distance between the plates, and the nature of the corresponding dominant modes. Finally, conclusions are drawn in Section 6.

2. Aerodynamic coupling of N flexible plates

2.1. Description of the problem

We are interested here in the linear stability of N horizontal identical flexible and inextensible plates, placed in a parallel imposed flow along the horizontal direction. The plates' span is assumed to be infinite so that the flow and plates' displacements can be considered two-dimensional. The plates are clamped at their leading edge and are equally spaced along the vertical axis at a distance D from each other: the leading edge of plate j ($1 \le j \le N$) is located at $(0,(j-1)D)$. All plates have length L in the streamwise direction, mass per unit area ρ_s and flexural rigidity $B = Eh^3/[12(1-\nu^2)]$ (per unit length in the third dimension). Here, E and ν are respectively the Young modulus and Poisson ratio of the plates, and h is the plate's thickness ($h \ll L$). The velocity and density of the imposed flow are ρ and U_∞. The problem is characterized by three nondimensional parameters (M^*, U^*, d) defined as

$$M^* = \frac{\rho L}{\rho_s}, \quad U^* = U_\infty L\sqrt{\frac{\rho_s}{B}}, \quad d = \frac{D}{L}. \tag{1}$$

In the following, all quantities are nondimensionalized using ρ, U_∞ and L as reference values: positions are nondimensionalized by L, time is nondimensionalized by L/U_∞, velocity by U_∞ and pressure by ρU_∞^2. We are interested in the linear stability of the state of rest for which all the plates are horizontal and parallel to the incoming flow.

Assuming that the displacement of each plate from its state of rest is small, the geometry of plate j is described by the vertical displacement $y^{(j)}(x,t)$ of the point located at a distance x along plate j in the state of rest. We are interested in the stability of infinitesimal perturbations, therefore $|y^{(j)}| \ll 1$. We assume that the plate is inextensible: any plate element must conserve its length at all time. Therefore, if $\xi^{(j)}(x,t)$ is the horizontal displacement of the point located at a distance x along plate j in the state of rest, the inextensibility of the plate can be expressed as

$$\left(1+\frac{\partial \xi^{(j)}}{\partial x}\right)^2 + \left(\frac{\partial y^{(j)}}{\partial x}\right)^2 = 1. \tag{2}$$

This relation implies that if $y^{(j)}$ is of order ε (with $\varepsilon \ll 1$), then the horizontal displacement $\xi^{(j)}(x,t)$ is of order ε^2, and we neglect this horizontal displacement here. Assuming that the dynamics is governed by the Euler–Bernoulli equation with clamped–free boundary conditions, and keeping only the dominant terms, the equation of motion of plate j is obtained as

$$\frac{\partial^2 y^{(j)}}{\partial t^2} = -\frac{1}{U^{*2}}\frac{\partial^4 y^{(j)}}{\partial x^4} - M^*[p]^{(j)}(x), \quad y^{(j)}(0,t) = y_x^{(j)}(0,t) = y_{xx}^{(j)}(1,t) = y_{xxx}^{(j)}(1,t) = 0, \tag{3}$$

where $[p]^{(j)}$ is the pressure difference between the upper and lower sides of plate j.

2.2. Potential flow and wake representation

The fluid domain is divided into $N+1$ domains (see Fig. 2):

(i) Domain 0: $y<0$,
(ii) Domain j ($1 \le j \le N-1$): $(j-1)d<y<jd$,
(iii) Domain N: $y>Nd$.

We assume that the flow is potential in all domains, and the flow potential is continuously differentiable in each domain. In (3), we have $[p]^{(j)}(x) = p^{(j)}(x,(j-1)d^+) - p^{(j-1)}(x,(j-1)d^-)$.

From the Bernoulli equation, the pressure in domain j is given by

$$p^{(j)}(x,y) = -\frac{\partial \Phi^{(j)}}{\partial t} - \frac{1}{2}|\nabla \Phi^{(j)}|^2, \tag{4}$$

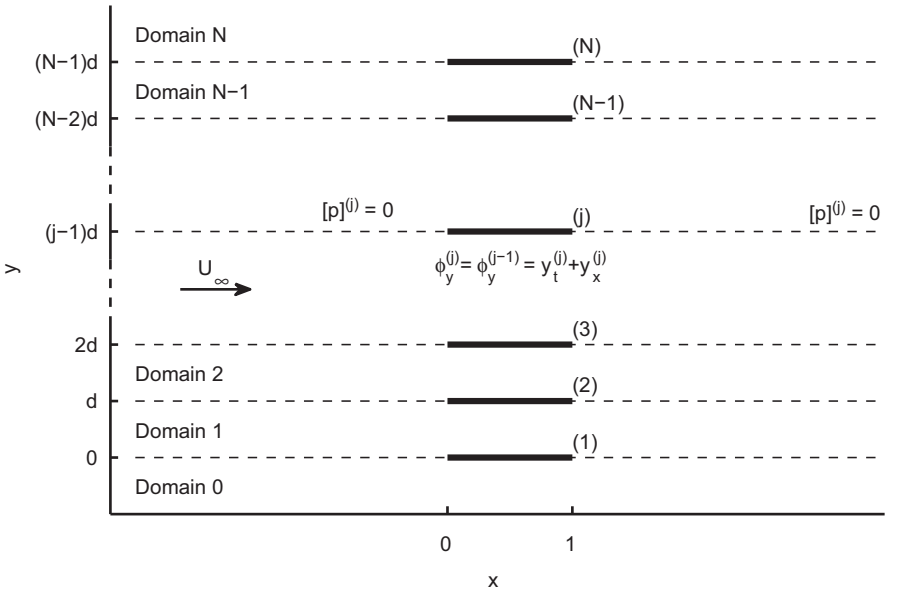

Fig. 2. Horizontal flow over N parallel plates. The plates index (j) is indicated as well as the $N+1$ domains in which the fluid is partitioned. On each plate, the continuity of the normal velocity is enforced. Continuity of pressure is enforced upstream and downstream along the direction of each plate.

where $\Phi^{(j)}$ is the total flow potential, which can be decomposed as

$$\Phi^{(j)}(x,y) = x + \phi^{(j)}(x,y) \tag{5}$$

with $\phi^{(j)}$ the perturbation of the potential due to the motion of the plates away from their state of rest ($|\nabla\phi^{(j)}| \ll 1$). Keeping only the linear terms, the pressure forcing on each plate becomes

$$[p]^{(j)}(x) = -\left(\frac{\partial}{\partial t} + \frac{\partial}{\partial x}\right)(\phi^{(j)} - \phi^{(j-1)}), \tag{6}$$

evaluated at $y = (j-1)d$.

The major difficulty in such situations is the representation of the wake. In the case of one single flapping plate, several models have been proposed. Using Theodorsen's (1935) theory (Bisplinghoff et al., 1955), Kornecki et al. (1976) represented the wake of a single flexible plate as a distribution of vorticity along the horizontal axis advected at leading order by the imposed flow. The intensity of the vorticity shed at each time was such that the regularity condition is enforced at the trailing edge. In the following, we refer to this method as the vortex sheet (VS) method. Computations with better accuracy *using the same method and assumptions* were reported recently (Eloy et al., 2008). The vortex sheet method was recently compared successfully to experimental and numerical results (Eloy et al., 2008; Michelin et al., 2008).

This elegant method is, however, difficult to generalize to two plates or one plate close to a wall, as it is based on the possibility of isolating the contribution of the frequency to the circulatory pressure with the so-called Theodorsen's function (Bisplinghoff et al., 1955). An alternative approach has been proposed, representing the presence of the wake by the continuity of the pressure across the horizontal axis downstream from the plate ($[p]^{(j)}(x) = 0$ for $x > 1$); Guo and Païdoussis (2000b) and Eloy et al. (2007) used this method to study, respectively, the two-dimensional stability of a plate with infinite span in an inviscid channel flow and the three-dimensional stability of a finite-span plate in an unbounded flow. In this method, the pressure distribution is solved in Fourier space and the absence of singularities at both edges is assumed, thereby introducing an "upstream wake" to deal with the leading edge singularity. In the following, we shall therefore refer to this method as the double wake (DW) approach.

Although this double-wake assumption is not based on any physical argument, it was observed that in the case of a single plate, it leads to a good prediction of the critical velocity for flutter instability (Eloy et al., 2007; Watanabe et al., 2002), particularly for lighter plates ($M^* \geq 1$). Fig. 3 shows that the velocity threshold obtained using the DW method is in good agreement with the prediction of the VS method for $M^* \geq 1$. Both methods (VS and DW) also predict the existence of different branches in the stability curve, each branch corresponding to different mode structures being most

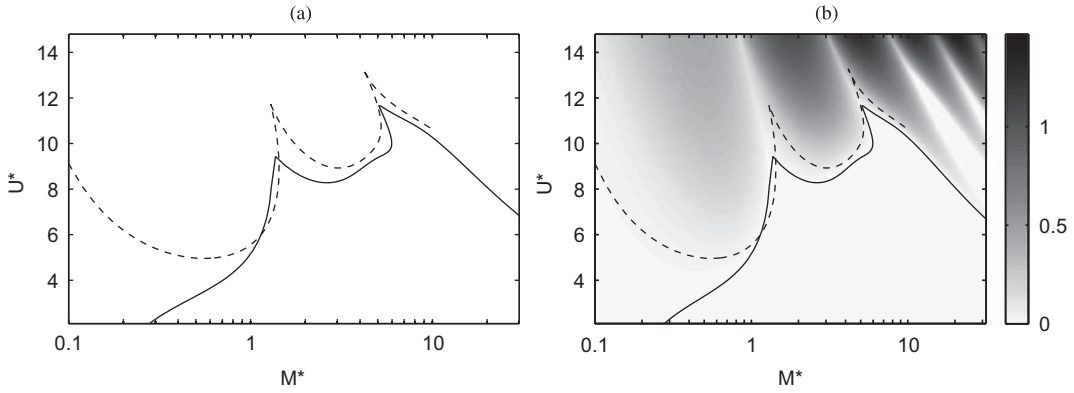

Fig. 3. (a) Critical stability curve of a single cantilevered flexible plate of infinite span using the double wake (DW) representation (solid) and using the vortex sheet (VS) wake model (dashed). (b) Stability curves of (a) superimposed on the maximum growth rate observed with the double wake representation.

unstable. The first branch corresponds to a mode 2 (one-neck mode), the second branch to a mode 3 (two-neck mode), and so on. Fig. 3(b) shows the superposition of the stability curves obtained with each method, and the maximum growth rate observed using the DW representation. This provides some insight on the behavior at small M^*. The VS model predicts a stable flat state while the DW predicts unstable behavior. However, the associated growth rates (obtained with the DW method) are very small in the region of disagreement between the two theories.

The difference between the two approaches resides solely in the treatment of the wake. At high values of M^*, the dominant modes have shorter wavelengths and it is therefore expected that their dynamics are less influenced by the wake and more by the local displacement of the plate. Conversely, the first branch has a characteristic spatial scale of the order of the length of the plate, and is strongly influenced by the description of the wake.

2.3. Computation of the pressure forcing

We follow the DW method to compute the pressure forcing on each plate (Guo and Païdoussis, 2000b; Eloy et al., 2007). Each plate's displacement is decomposed into normal modes $y^{(j)}(x,t) = \mathrm{Re}[\zeta^{(j)}(x)\mathrm{e}^{\mathrm{i}\omega t}]$ with ω *a priori* complex. $\mathrm{Re}(\omega)$ and $-\mathrm{Im}(\omega)$ are respectively the mode's frequency and growth rate. Unstable modes correspond to positive growth rate ($\mathrm{Im}(\omega)<0$) and stable modes to negative growth rate ($\mathrm{Im}(\omega)>0$). All quantities (pressure, potential) are also proportional to $\mathrm{e}^{\mathrm{i}\omega t}$, and in the following the time-dependence $\mathrm{e}^{\mathrm{i}\omega t}$ will be implicit. The flow potential must satisfy the following system:

$$\nabla^2\phi^{(j)} = \frac{\partial^2\phi^{(j)}}{\partial x^2} + \frac{\partial^2\phi^{(j)}}{\partial y^2} = 0, \quad 0 \le j \le N, \tag{7a}$$

$$\nabla\phi^{(0)}|_{y\to-\infty} = \nabla\phi^{(N)}|_{y\to\infty} = 0, \tag{7b}$$

$$\frac{\partial\phi^{(j-1)}}{\partial y}(x, y=(j-1)d) = \frac{\partial\phi^{(j)}}{\partial y}(x, y=(j-1)d) = \mathrm{i}\omega\zeta^{(j)} + \frac{\mathrm{d}\zeta^{(j)}}{\mathrm{d}x} \quad \text{for } 0 \le x \le 1, \tag{7c}$$

$$[p]^{(j)}(x) = 0 \quad \text{for } x \le 0 \text{ and } x \ge 1, \tag{7d}$$

with the pressure jump obtained from Bernoulli's equation (6) as

$$[p]^{(j)}(x) = -\left(\mathrm{i}\omega + \frac{\mathrm{d}}{\mathrm{d}x}\right)[\phi^{(j)}(x,(j-1)d) - \phi^{(j-1)}(x,(j-1)d)]. \tag{8}$$

Eq. (7b) prescribes the correct decay of the flow perturbation: far from the plates in domain (0) and (N), the velocity is dominated by the imposed unit parallel flow, and the perturbation velocity becomes negligible. Condition (7c) enforces the slip boundary condition on each plate: on each side of the plate, the normal velocity of the flow must be equal to the plate's normal velocity. Eq. (7d) is the regularity condition introduced by the wake downstream of the plates and the fictitious upstream wake: from (8), we see that it is equivalent to the advection by the mean flow of a discontinuity in the flow potential, or equivalently of a vorticity distribution on the horizontal axis (Eloy et al., 2007).

Using the Fourier transform in x, we look for solutions of the form

$$\phi^{(j)}(x,y) = \int_{-\infty}^{\infty} \tilde{\phi}^{(j)}(k,y) \mathrm{e}^{\mathrm{i}kx}\,\mathrm{d}k, \tag{9}$$

and from (7a) the function $\tilde{\phi}^{(j)}(k,y)$ must satisfy

$$\frac{\partial^2 \tilde{\phi}^{(j)}}{\partial y^2} - k^2 \tilde{\phi}^{(j)} = 0, \tag{10}$$

whose general solution can be written as

$$\tilde{\phi}^{(j)}(k,y) = A^{(j)}(k)\mathrm{e}^{-|k|y} + B^{(j)}(k)\mathrm{e}^{|k|y}. \tag{11}$$

From (7c), we obtain

$$B^{(j)}(k) - A^{(j)}(k)\mathrm{e}^{-2|k|(j-1)d} = B^{(j-1)}(k) - A^{(j-1)}(k)\mathrm{e}^{-2|k|(j-1)d} \quad \text{for } 1 \le j \le N. \tag{12}$$

The pressure difference at $y = (j-1)d$ is then computed from (8) and (12) as

$$[p]^{(j)}(x) = -2\mathrm{i}\int_{-\infty}^{\infty} (\omega + k)[A^{(j)}(k) - A^{(j-1)}(k)]\mathrm{e}^{-|k|(j-1)d}\mathrm{e}^{\mathrm{i}kx}\,\mathrm{d}k \tag{13a}$$

$$= -2\mathrm{i}\int_{-\infty}^{\infty} (\omega + k)[B^{(j)}(k) - B^{(j-1)}(k)]\mathrm{e}^{|k|(j-1)d}\mathrm{e}^{\mathrm{i}kx}\,\mathrm{d}k. \tag{13b}$$

Differentiating (13) with respect to x and using the inverse Fourier transform and (7d), we obtain

$$A^{(j)}(k) - A^{(j-1)}(k) = \frac{\mathrm{e}^{|k|(j-1)d}}{4\pi k(\omega + k)} \int_0^1 [p]'^{(j)}(\xi)\mathrm{e}^{-\mathrm{i}k\xi}\,\mathrm{d}\xi, \tag{14a}$$

$$B^{(j)}(k) - B^{(j-1)}(k) = \frac{\mathrm{e}^{-|k|(j-1)d}}{4\pi k(\omega + k)} \int_0^1 [p]'^{(j)}(\xi)\mathrm{e}^{-\mathrm{i}k\xi}\,\mathrm{d}\xi, \tag{14b}$$

where the prime denotes a derivative with respect to x ($[p]'^{(j)}$ is therefore the horizontal gradient of the pressure jump on plate j). Using (7b), $A^{(0)} = B^{(N)} = 0$ and therefore

$$A^{(j)}(k) = \frac{1}{4\pi k(\omega + k)} \sum_{l=1}^{j} \mathrm{e}^{|k|(l-1)d} \int_0^1 [p]'^{(l)}(\xi)\mathrm{e}^{-\mathrm{i}k\xi}\,\mathrm{d}\xi, \tag{15a}$$

$$B^{(j)}(k) = \frac{-1}{4\pi k(\omega + k)} \sum_{l=j+1}^{N} \mathrm{e}^{-|k|(l-1)d} \int_0^1 [p]'^{(l)}(\xi)\mathrm{e}^{-\mathrm{i}k\xi}\,\mathrm{d}\xi. \tag{15b}$$

Finally, applying the operator $(\mathrm{i}\omega + \mathrm{d}/\mathrm{d}x)$ to (7c), and using (11) and (15),

$$\begin{aligned} -\omega^2\zeta^{(j)} + 2\mathrm{i}\omega\frac{\mathrm{d}\zeta^{(j)}}{\mathrm{d}x} + \frac{\mathrm{d}^2\zeta^{(j)}}{\mathrm{d}x^2} &= \mathrm{i}\int_{-\infty}^{\infty} |k|(\omega + k)(B^{(j)}\mathrm{e}^{|k|(j-1)d} - A^{(j)}\mathrm{e}^{-|k|(j-1)d})\mathrm{e}^{\mathrm{i}kx}\,\mathrm{d}k \\ &= -\frac{\mathrm{i}}{4\pi}\int_{-\infty}^{\infty} \mathrm{sgn}(k) \sum_{l=1}^{N} \mathrm{e}^{-|k(j-l)|d} \int_0^1 [p]'^{(l)}(\xi)\mathrm{e}^{\mathrm{i}k(x-\xi)}\,\mathrm{d}\xi\,\mathrm{d}k \\ &= \frac{1}{2\pi}\sum_{l=1}^{N}\int_0^1 K_{j,l}(x-\xi)[p]'^{(l)}(\xi)\,\mathrm{d}\xi \end{aligned} \tag{16}$$

with

$$K_{j,l}(u) = -\frac{\mathrm{i}}{2}\int_{-\infty}^{\infty} \mathrm{sgn}(k)\mathrm{e}^{-|k(j-l)|d}\mathrm{e}^{\mathrm{i}ku}\,\mathrm{d}k. \tag{17}$$

Using the following pair of Fourier transforms:

$$-\frac{\mathrm{i}}{2}\mathrm{sgn}(k) \longleftrightarrow \frac{1}{u}, \quad \mathrm{e}^{-|k|\alpha} \longleftrightarrow \frac{2\alpha}{\alpha^2 + u^2}, \tag{18}$$

we obtain

$$K_{j,l}(u) = \frac{u}{u^2 + (j-l)^2 d^2} \quad \text{for } 1 \le \{j,l\} \le N. \tag{19}$$

We therefore have to solve the following system of integral equations for the pressure gradients along each plate $[p]'^{(j)}$:

$$\frac{1}{2\pi}\int_0^1 \frac{[p]'^{(j)}(\xi)\,\mathrm{d}\xi}{x-\xi}+\frac{1}{2\pi}\sum_{l\neq j}\int_0^1 \frac{x-\xi}{(x-\xi)^2+(j-l)^2d^2}[p]'^{(l)}(\xi)\,\mathrm{d}\xi=-\omega^2\zeta^{(j)}+2\mathrm{i}\omega\frac{\mathrm{d}\zeta^{(j)}}{\mathrm{d}x}+\frac{\mathrm{d}^2\zeta^{(j)}}{\mathrm{d}x^2}, \tag{20}$$

for $1\leq j\leq N$, with the additional constraints that $[p]^{(j)}=0$ at $x=\{0,1\}$ so that $\int_0^1[p]'^{(j)}\,\mathrm{d}x=0$. In (20), we have purposedly isolated the term $j=l$ which gives a Cauchy-type singular kernel. The first integral is understood as the Cauchy principal value. The linearity and form of (20) suggests to look for a solution of this system of integral equations in the following form (see for example Eloy et al., 2007):

$$[p]^{(j)}(x)=[p^{(K)}]^{(j)}(x)+2\mathrm{i}\omega[p^{(G)}]^{(j)}(x)-\omega^2[p^{(M)}]^{(j)}(x) \tag{21}$$

with $0\leq x\leq 1$ and $1\leq j\leq N$. The pressure forcings $[p^{(K)}]^{(j)}$, $[p^{(G)}]^{(j)}$ and $[p^{(M)}]^{(j)}$ are solutions of

$$\frac{1}{2\pi}\int_0^1 \frac{[p^{(K)}]'^{(j)}(\xi)\,\mathrm{d}\xi}{x-\xi}+\frac{1}{2\pi}\sum_{l\neq j}\int_0^1 \frac{x-\xi}{(x-\xi)^2+(j-l)^2d^2}[p^{(K)}]'^{(l)}(\xi)\,\mathrm{d}\xi=\frac{\mathrm{d}^2\zeta^{(j)}}{\mathrm{d}x^2}\quad\text{with}\quad\int_0^1[p^{(K)}]'^{(j)}\,\mathrm{d}x=0, \tag{22a}$$

$$\frac{1}{2\pi}\int_0^1 \frac{[p^{(G)}]'^{(j)}(\xi)\,\mathrm{d}\xi}{x-\xi}+\frac{1}{2\pi}\sum_{l\neq j}\int_0^1 \frac{x-\xi}{(x-\xi)^2+(j-l)^2d^2}[p^{(G)}]'^{(l)}(\xi)\,\mathrm{d}\xi=\frac{\mathrm{d}\zeta^{(j)}}{\mathrm{d}x}\quad\text{with}\quad\int_0^1[p^{(G)}]'^{(j)}\,\mathrm{d}x=0, \tag{22b}$$

$$\frac{1}{2\pi}\int_0^1 \frac{[p^{(M)}]'^{(j)}(\xi)\,\mathrm{d}\xi}{x-\xi}+\frac{1}{2\pi}\sum_{l\neq j}\int_0^1 \frac{x-\xi}{(x-\xi)^2+(j-l)^2d^2}[p^{(M)}]'^{(l)}(\xi)\,\mathrm{d}\xi=\zeta^{(j)}\quad\text{with}\quad\int_0^1[p^{(M)}]'^{(j)}\,\mathrm{d}x=0. \tag{22c}$$

In (21) and (22), the pressure contributions with superscripts K, G and M correspond respectively to added rigidity, gyroscopic and added inertia effects (Païdoussis, 2004).

2.4. Galerkin decomposition

The stability problem is then investigated using the Galerkin method. The displacement of each plate is decomposed onto the Q first normal modes of the clamped–free beam in vacuum

$$\zeta^{(j)}(x)=\sum_{n=1}^{Q}\alpha_n^{(j)}\psi_n(x),\quad \psi_n(x)=\cosh(\lambda_n x)-\cos(\lambda_n x)+\frac{\sin(\lambda_n)-\sinh(\lambda_n)}{\cos(\lambda_n)+\cosh(\lambda_n)}[\sinh(\lambda_n x)-\sin(\lambda_n x)], \tag{23}$$

and λ_n are the successive positive roots of

$$1+\cos\lambda_n\cosh\lambda_n=0. \tag{24}$$

These modes are solutions of the following problem:

$$\frac{\mathrm{d}^4\psi_n}{\mathrm{d}x^4}=\lambda_n^4\psi_n,\quad \psi_n(0)=\psi_n'(0)=\psi_n''(1)=\psi_n'''(1)=0. \tag{25}$$

From this basis for one plate, we can easily build the basis for the N-plate problem by considering the modes Ψ_m ($1\leq m\leq N\times Q$) defined as follows: mode $(i-1)Q+q$ (with $1\leq q\leq Q$ and $1\leq i\leq N$) corresponds to a displacement equal to ψ_q for plate i, all the other plates being held fixed. (In other words, if $\boldsymbol{\psi}$ is the matrix of the value of the modes (23) at a set of points $\mathbf{x}$, the basis $\boldsymbol{\Psi}$ for the N-plate problem is block-diagonal with N diagonal blocks equal to $\boldsymbol{\psi}$.)

From (21), for each mode Ψ_m, we obtain the pressure gradient P'_m as the following superposition:

$$P'_m=P'^{(K)}_m+2\mathrm{i}\omega P'^{(G)}_m-\omega^2P'^{(M)}_m, \tag{26}$$

with $P^{(K)}_m=[[p^{(K)}]^{(1)}_m,[p^{(K)}]^{(2)}_m,\ldots,[p^{(K)}]^{(N)}_m]^{\mathrm{T}}$ and from (22),

$$\frac{1}{2\pi}\int_0^1 \frac{[p^{(K)}]'^{(j)}_m(\xi)\,\mathrm{d}\xi}{x-\xi}+\frac{1}{2\pi}\sum_{l\neq j}\int_0^1 \frac{x-\xi}{(x-\xi)^2+(j-l)^2d^2}[p^{(K)}]'^{(l)}_m(\xi)\,\mathrm{d}\xi=\frac{\mathrm{d}^2\Psi^{(j)}_m}{\mathrm{d}x^2},$$

$$\int_0^1[p^{(K)}]'^{(j)}_m(x)\,\mathrm{d}x=0 \tag{27}$$

with $\Psi^{(j)}_{(i-1)Q+q}(x)=\delta_{ij}\psi_q(x)$. $P'^{(G)}_m$ and $P'^{(M)}_m$ are obtained in the same way from (22), and the different pressure fields are then recovered by integration from the leading edge.

For the N plates, Eq. (3) becomes (noting that most of the coefficients of each Ψ_m are zero):

$$\sum_{m=1}^{N\times Q}\alpha_m\left[-\omega^2\Psi_m+\frac{1}{U^{*2}}\frac{\mathrm{d}^4\Psi_m}{\mathrm{d}x^4}+M^*(-\omega^2P_m^{(M)}+2\mathrm{i}\omega P_m^{(G)}+P_m^{(K)})\right]=0. \tag{28}$$

We define the scalar product $\langle\cdot\rangle$ of $F=[f^{(1)}(x),\ldots,f^{(N)}(x)]^{\mathrm{T}}$ and $G=[g^{(1)}(x),\ldots,g^{(N)}(x)]^{\mathrm{T}}$ as

$$\langle F,G\rangle=\sum_{j=1}^{N}\int_0^1 f^{(j)}(x)g^{(j)}(x)\,\mathrm{d}x. \tag{29}$$

Taking the scalar product of (28) with Ψ_n, we obtain a nonlinear eigenvalue problem in ω:

$$\left[-\omega^2(\mathbf{M}+M^*\mathbf{F^{(M)}})+2\mathrm{i}\omega M^*\mathbf{F^{(G)}}+\frac{1}{U^{*2}}\mathbf{K}+M^*\mathbf{F^{(K)}}\right]\cdot\boldsymbol{\alpha}=0, \tag{30}$$

where

$$\begin{aligned}&M_{mn}=\langle\Psi_m,\Psi_n\rangle,\quad K_{mn}=\left\langle\frac{\mathrm{d}^4\Psi_m}{\mathrm{d}x^4},\Psi_n\right\rangle,\\&F_{mn}^{(M)}=\langle P_m^{(M)},\Psi_n\rangle,\quad F_{mn}^{(G)}=\langle P_m^{(G)},\Psi_n\rangle,\quad F_{mn}^{(K)}=\langle P_m^{(K)},\Psi_n\rangle.\end{aligned} \tag{31}$$

Because $\Psi_{(i-1)Q+q}^{(j)}=\delta_{ij}\psi_p(x)$, and the natural modes of the clamped–free beam are orthogonal and satisfy (25), $\mathbf{M}$ is the identity matrix and $\mathbf{K}$ is diagonal with

$$K_{(i-1)Q+q}=\lambda_q^4\quad\text{for } 1\le i\le N \text{ and } 1\le q\le Q, \tag{32}$$

with λ_q defined in (24).

2.5. Numerical solution

The main task consists in determining the matrices $\mathbf{F^{(M)}}$, $\mathbf{F^{(G)}}$ and $\mathbf{F^{(K)}}$. The results presented thereafter were obtained using $Q=24$ modes for each plate. A large enough number of Galerkin modes must be used to properly resolve the structure, growth rate and frequency of the physical modes [see for example Lemaitre et al. (2005)], and tests with $Q=48$ and 96 were performed to ensure a proper convergence. Eq. (30) has $N_{\mathrm{tot}}=2N\times Q$ eigenmodes and the modes with largest frequency arise from the Galerkin decomposition and are not physical. We therefore chose to retain only the $N_{\mathrm{tot}}/4$ modes with smallest frequency in the remainder of the paper ($12N$ modes for $Q=24$) to ensure we are studying only physical modes. This choice might lead us to discard some physical modes, but such discarded modes would have a very high frequency and short wavelength. Therefore, we expect these modes to have a negligible effect in the analysis of the real problem, as flow viscosity and material damping (both neglected in the present potential flow approach) would lead to a rapid dissipation of the energy in those modes.

Each function $\psi_n(x)$ is evaluated on $N_p=200$ Gauss–Chebyshev points, and expanded using the first N_p Chebyshev polynomials of the first kind. Using this discretization is particularly well-suited for the solution of the coupled singular integral equations (22). The procedure for solving (22) is detailed in Appendix A. Once the different $[p^{(K)}]^{(j)}$, $[p^{(G)}]^{(j)}$ and $[p^{(M)}]^{(j)}$ have been obtained, the matrix coefficients are computed using (29) and a Gauss–Chebyshev quadrature (Pozrikidis, 1998).

Once the matrices $\mathbf{F^{(M)}}$, $\mathbf{F^{(G)}}$ and $\mathbf{F^{(K)}}$ have been obtained for a given value of d, the nonlinear eigenvalue problem (30) is solved for given values of M^* and U^*.

We first note that, in (30), ω always appears as powers of $\mathrm{i}\omega$ and all matrices are real. Therefore, if ω is a solution, $-\bar{\omega}$ is as well, with the same mode structure characteristics (the eigenfunctions are conjugate pairs). This result is a direct consequence of the choice made for the modal decomposition: $y^{(j)}(x,t)=\mathrm{Re}[\zeta^{(j)}(x)\mathrm{e}^{\mathrm{i}\omega t}]$. The eigenvalues are therefore of two kinds: purely imaginary and pairs of eigenvalues with the same imaginary parts but opposite real parts. Because of this structure, in the following we will only discuss the eigenvalue with positive real part, keeping in mind that when this real part is strictly positive, an associated eigenvalue also exists with opposite real part.

In the following, we study successively the stability properties of $N=2$, $N=3$ and $N\gg1$ parallel elastic plates. In several places, we will consider the most unstable mode to determine for example the dominant mode's nature. We must point out here that this mode is dominant in the linear regime. Although several numerical and experimental studies on flexible flags have reported a good agreement between the structure of the observed dominant mode and the prediction of linear stability analysis [e.g. Eloy et al. (2008), Michelin et al. (2008)], in the fully developed regime, nonlinear phenomena such as mode competition could modify the nature or properties of the dominant mode (e.g. frequency).

This will therefore limit our ability to perform a quantitative comparison of our linear stability results to the experimental work of Zhang et al. (2000) and Jia et al. (2007), as the motion of the filaments observed in these experiments correspond to a fully developed nonlinear regime. Furthermore, although soap-film experiments represent a good approximation of two-dimensional flows, this approximation is only valid far from the filaments: the wetting of the filaments creates a bulge of fluid whose influence on the inertia and rigidity of the filament can only be estimated roughly [see Zhu and Peskin (2003)]. A qualitative comparison of the mode nature and properties with the experimental observations can however be performed.

3. Stability of two coupled plates

In this section, we focus on the case of two identical flexible plates placed at a relative distance d from each other. The method outlined in the previous section is used setting $N = 2$.

3.1. Influence of d on the stability of the flat state of rest

One question of interest when approaching two flexible plates to each other is whether and how the presence of the other plate will influence the stability threshold of the state of rest (flat and parallel to the imposed flow). The critical stability curve is plotted in Fig. 4 for various values of the relative distance between the plates' leading edges. Below the critical curve, the state of rest is a stable equilibrium; above it, this state of rest is unstable and flapping can develop.

As a general result, we observe that the hydrodynamic coupling between the plates tends to destabilize the state of rest, as the stable range of parameter values (M^*, U^*) shrinks with decreasing d. We observe that this reduction of the stability threshold $U_c(M^*, d)$ with d (or the minimum U^* above which the state of rest becomes unstable) is not uniform with respect to M^*. Heavy flags ($M^* \leq 1$) are destabilized for distances between the plates as large as three times their lengths, while the stability of light plates ($M^* \geq 5$) is not affected until $d < 0.5$.

This is confirmed by looking at the growth rate of the most unstable mode, plotted in Fig. 5(a) for several values of the relative distance between the plates. Two effects are evident from this picture. As expected for a particular distance d, the growth rate increases above the critical stability curve for increasing U^*: increasing U^* corresponds to an increasing forcing flow or a relatively smaller rigidity of the plates. More kinetic energy is then transferred from the outside flow to the plates' motion.

For small d, the dominant mode's stability properties are modified the most for small M^*: in that case, a significant increase of the dominant mode's growth rate is observed for decreasing d. The comparison of the different pictures in Fig. 5(a) also shows the evolution with d of the location of branches with reduced instability (light colors) in the (M^*, U^*)-plane, information that is not available when only the critical stability curve is considered. These regions are the most susceptible to become stable if a small amount of dissipation is added to the system.

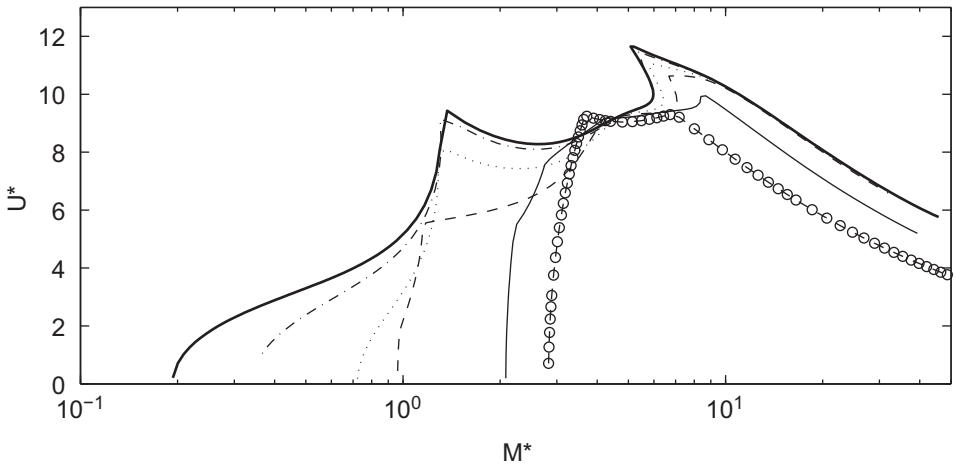

Fig. 4. Critical stability curve of the state of rest of two plates in the (M^*, U^*)-plane for $d = 0.1$ (circle), $d = 0.2$ (thin solid), $d = 0.5$ (dashed), $d = 1$ (dotted) and $d = 3$ (dash-dotted). The thick solid line is the stability curve for one flag only using the same approach (Eloy et al., 2007) and is equivalent to $d = \infty$.

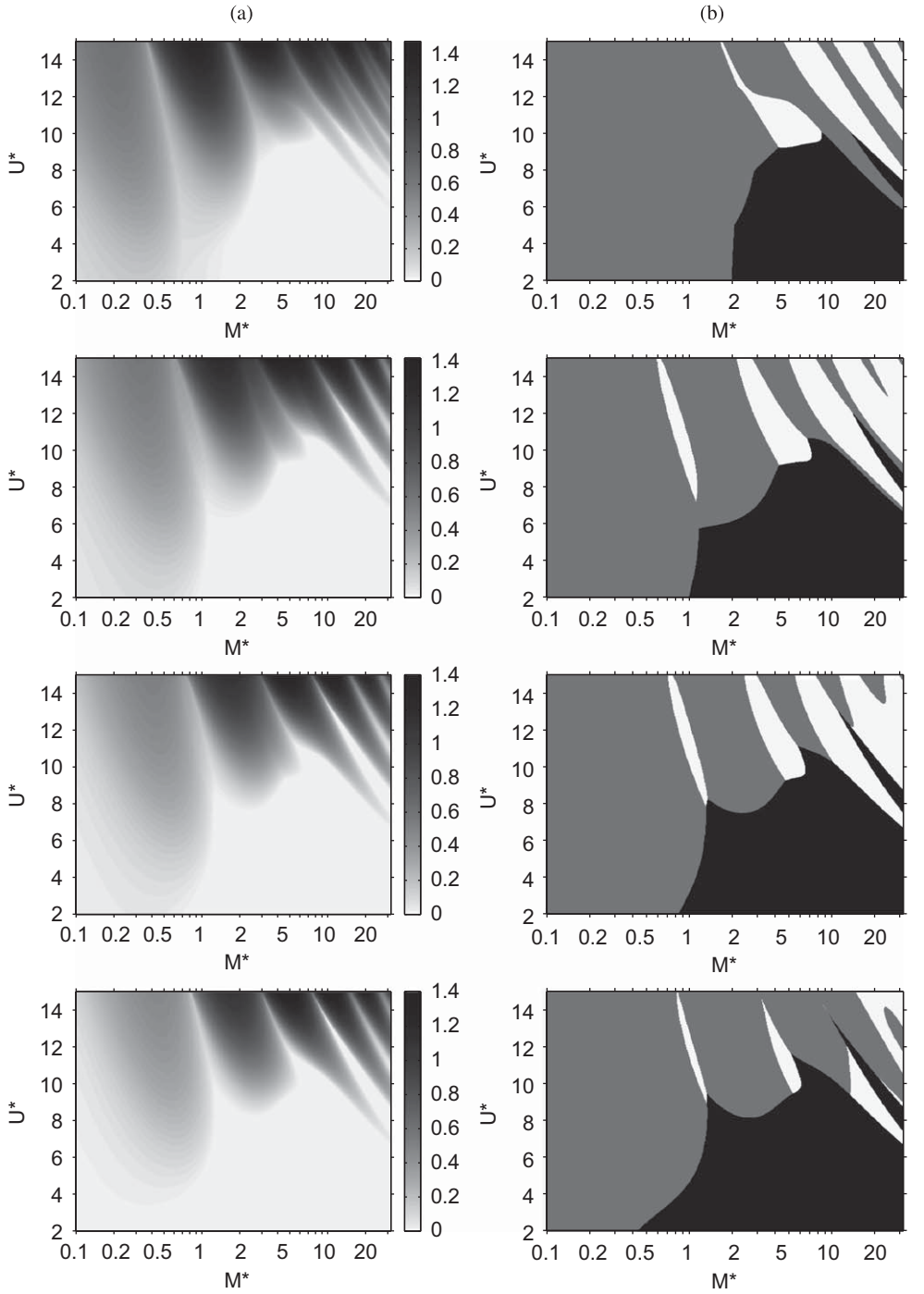

Fig. 5. (a) Growth rate and (b) nature of the most unstable mode plotted in the (M^*, U^*)-plane for (from top to bottom) $d = 0.2, 0.5, 1$ and 3. On the right column, the stability region of the state of rest is shown in black, while grey (resp. white) regions correspond to an out-of-phase (resp. in-phase) dominant mode.

This difference of behavior between small M^* and large M^* is illustrated in Fig. 6 where the dominant mode characteristics are studied in the (U^*, d)-plane. For $M^* = 2$, the dominant mode stability, nature, growth rate and frequency depend strongly on d, while for $M^* = 4$, d has a much weaker influence and the frequency and growth rate variations are due to changes in the dominant mode rather than a modification of a particular mode's properties with d.

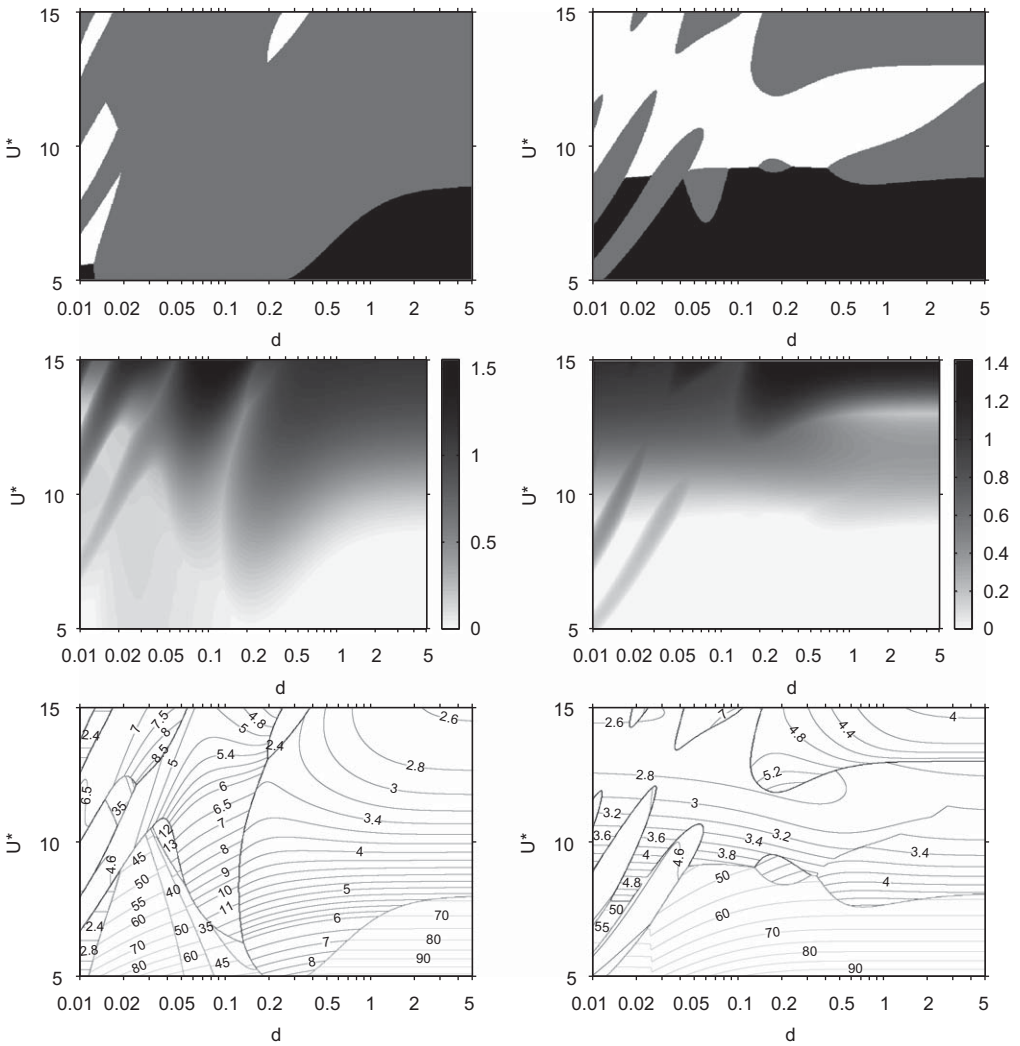

Fig. 6. Evolution of the dominant mode properties in the (d, U^*)-plane for $M^* = 2$ (left) and $M^* = 4$ (right). (Top) Regime observed (with the same color code as in Fig. 5). (Center) Growth rate of the most unstable mode (stable regions are indicated with a zero growth rate). (Bottom) Frequency of the dominant mode.

One interpretation of the preferential destabilization of flags with low M^* lies in the mode structure associated with each branch on the stability curves in Figs. 3 and 4. The most unstable branch at low M^* corresponds to modes with longer wavelengths than the subsequent branches. Modes with shorter wavelengths are expected to be less influenced by the presence of the second plate as the relevant aspect ratio is λ/D rather than L/D for this particular mode, with λ the wavelength of the mode.

3.2. In-phase and out-of-phase modes

For two coupled plates, eigenmodes can be of two natures: in-phase (the two plates having the same motion) and out-of-phase (the two plates having symmetric motions with respect to the horizontal axis) as illustrated in Figs. 1 and 7. The nature of the mode is determined by computing the correlation between the spatial structure of the mode component along each plate. For a particular mode ω, each plate's displacement can be defined as $y^{(j)}(x,t) = \mathrm{Re}[\zeta^{(j)}(x)e^{i\omega t}]$ with the same complex frequency ω. The correlation coefficient for the motion of plates m and n is defined

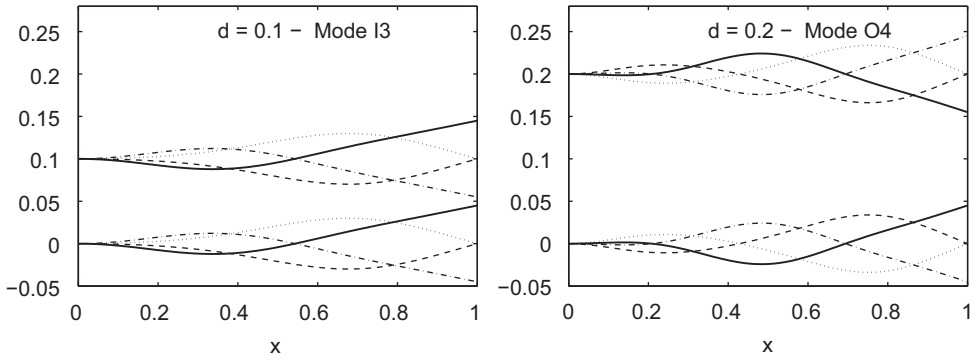

Fig. 7. Dominant mode for $M^* = 4$ and $U^* = 13$ for (left) $d = 0.1$ and (right) $d = 0.2$. The position of each plate is plotted at $t = t_0$ (solid), $t = t_0 + T/4$ (dashed), $t = t_0 + T/2$ (dash-dotted) and $t = t_0 + 3T/4$ (dotted), with T the pseudo-period of the mode ($2\pi/\mathrm{Re}(\omega)$). The same arbitrary amplitude of vertical motion was chosen for both cases.

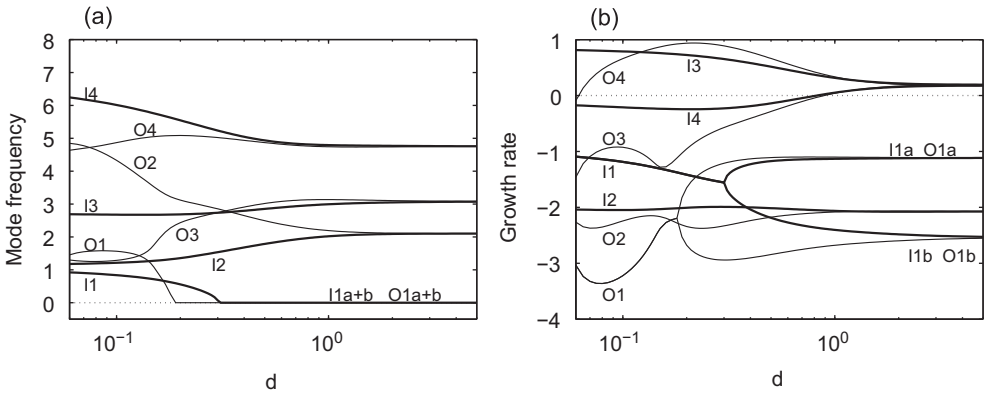

Fig. 8. $M^* = 4$ and $U^* = 13$. Variations of (a) the frequency and (b) the growth rate of the four in-phase (thick lines) and out-of-phase (thin lines) least stable modes. The modes are numbered by increasing frequency in the limit $d \to \infty$.

as the average value in x of the time correlation of these plates' displacement at x:

$$r_{mn} = \int_0^1 \frac{\mathrm{Re}[\zeta^{(m)}(x)\overline{\zeta^{(n)}(x)}]}{|\zeta^{(m)}(x)\zeta^{(n)}(x)|}\,\mathrm{d}x, \tag{33}$$

where the integrand is just the relative phase between $\zeta^{(m)}(x)$ and $\zeta^{(n)}(x)$. This definition remains valid for the case of multiple plates. Here there are only two plates and only one correlation $r = r_{12}$. In practice, within each mode of the two-plate system, the displacements of the plates were found either equal or opposite and a symmetry argument for this is given in Section 5. Therefore, the correlation coefficient r is equal to ± 1. A mode with $r = 1$ (resp. $r = -1$) is called thereafter an *in-phase* (resp. *out-of-phase*) mode. Fig. 5(b) shows for given values of d, the nature of the most unstable mode in the (M^*, U^*)-plane. Alternatively, Fig. 6 shows the evolution of the nature of the dominant mode in the (d, U^*)-plane for given M^*, thereby giving some insight on the influence of d.

In the following, modes will be referenced by their nature (I for in-phase modes and O for out-of-phase modes) and numbered by increasing frequencies at large d, to correspond for convenience to the numbering of the one-plate case (it is therefore possible for a mode 2 to have a higher frequency than a mode 3 at shorter distances).

These maps show that for increasing d, the domain of stability of the flat state of rest increases, as observed in the previous section. From Figs. 5 and 6, we also observe that for given values of M^* and U^*, it is possible to observe an in-phase mode at small distances d and a transition to an out-of-phase regime for increasing plate separation (see for example the case $M^* = 4$ and $U^* = 13$ in Fig. 6 and in more detail in Fig. 8). This transition from in-phase to out-of-phase modes with increasing separation was observed experimentally (Zhang et al., 2000; Jia et al., 2007).

While it is clear from Fig. 5(b) that the in-phase flapping modes are more often dominant at small distances than at larger distances, this transition is not always observed: in-phase flapping can be observed for large d (up to five times the plate's length for $M^*=4$ and $U^*=12.5$ as seen in Fig. 6) and out-of-phase flapping can be observed for all values of d (for small inertia ratio M^*, the dominant mode is always out-of-phase). This is consistent with the soap-film experiments reported in Jia et al. (2007), which observed an out-of-phase mode at small and large distances for the shortest filament length (corresponding to smaller M^* and U^*, if all other properties are kept constant). It is also consistent with the results of Tang and Païdoussis (2009), who observed that the velocity threshold of the fluttering instability was always lower for out-of-phase modes than for in-phase modes in their study of plates with $M^*=0.2$.

3.3. Influence of d on the mode properties

Figs. 8 and 9 show the evolution with d of the frequency $\mathrm{Re}(\omega)$ and growth rate $\mathrm{Im}(-\omega)$ of the lowest frequency in-phase and out-of-phase modes for two different sets of values of (M^*, U^*). The branches on each of these plots correspond to continuous variations of the eigenvalue ω. Note also that the nature of the mode (in-phase/out-of-phase) remains unchanged on a particular branch for all d-values (the correlation coefficient for each branch remains very close to either 1 or -1).

The structure of the mode (e.g. number of necks) can however vary with d, although we note that the most unstable modes preserve their general structure throughout the d-domain (Fig. 10). Other more damped modes can however experience a strong modification of their structure as can be seen for mode O1b for example in Fig. 10. The existence of a zero in the envelope corresponds to a standing wave mode ($\mathrm{Re}(\omega)=0$).

At large distances, we observe the pairing of in-phase and out-of-phase branches. Within each pair, the mode frequencies, growth rates and mode structures become identical and approach asymptotically the mode characteristics obtained in the case of a single plate (Figs. 8 and 10). Within each pair, the two modes differ however by the values of the correlation coefficient r (or the phase difference between the plates' motion) which are opposite.

We showed that the variations of the modes' growth rate with d, M^* and U^* can induce a sudden change of the dominant mode nature as one parameter is varied (corresponding to the different domain boundaries in Figs. 5(b) and 6). If the most linearly unstable mode determines the properties of the observed flapping in experiments and numerical simulations, then by varying one of the parameters (by either changing the separation D or the flow velocity U_∞ for example), one will experience a sudden change in the observed properties (for example, the flapping mode shape or its frequency). For $M^*=4$ and $U^*=13$, the dominant mode is an in-phase flapping at short distances ($d<0.15$) and an out-of-phase flapping at larger distances (Fig. 8). At the transition, the structure of the dominant mode (and therefore its characteristic wavelength) is also modified from a 2-neck mode (I3) to a 3-neck mode (O4) (see Fig. 7), and a frequency jump is observed from $\omega=2.68$ (mode I3) to $\omega=4.96$ (mode I4). This frequency switch was also reported in previous experimental and numerical studies (Zhang et al., 2000; Farnell et al., 2004; Jia et al., 2007).

The frequency jump can be observed even when a transition occurs between two modes of the same nature. Fig. 9 illustrates this with a case where an out-of-phase mode is always dominant for $M^*=2$ and $U^*=10$. Mode O4 is dominant for small distances d, while O3 is dominant at larger distances. The mode switch at $d\sim0.13$ leads to a negative dominant frequency switch from $\omega=8.1$ to 3.7.

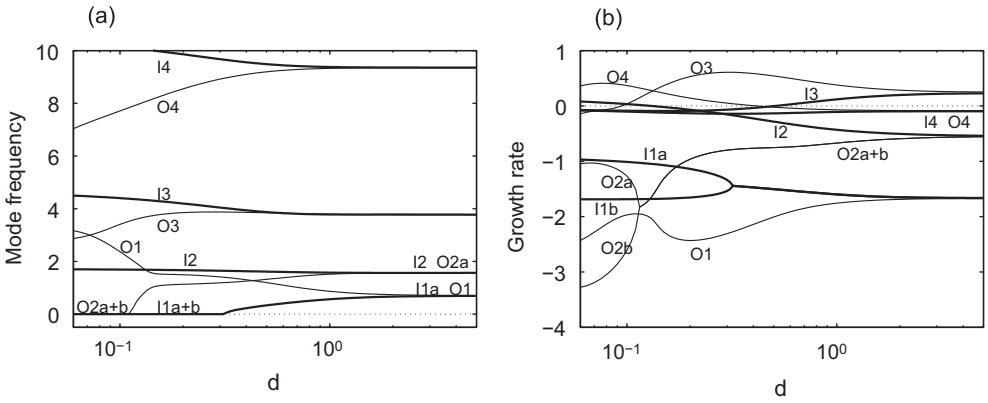

Fig. 9. Same as Fig. 8 for $M^*=2$ and $U^*=10$.

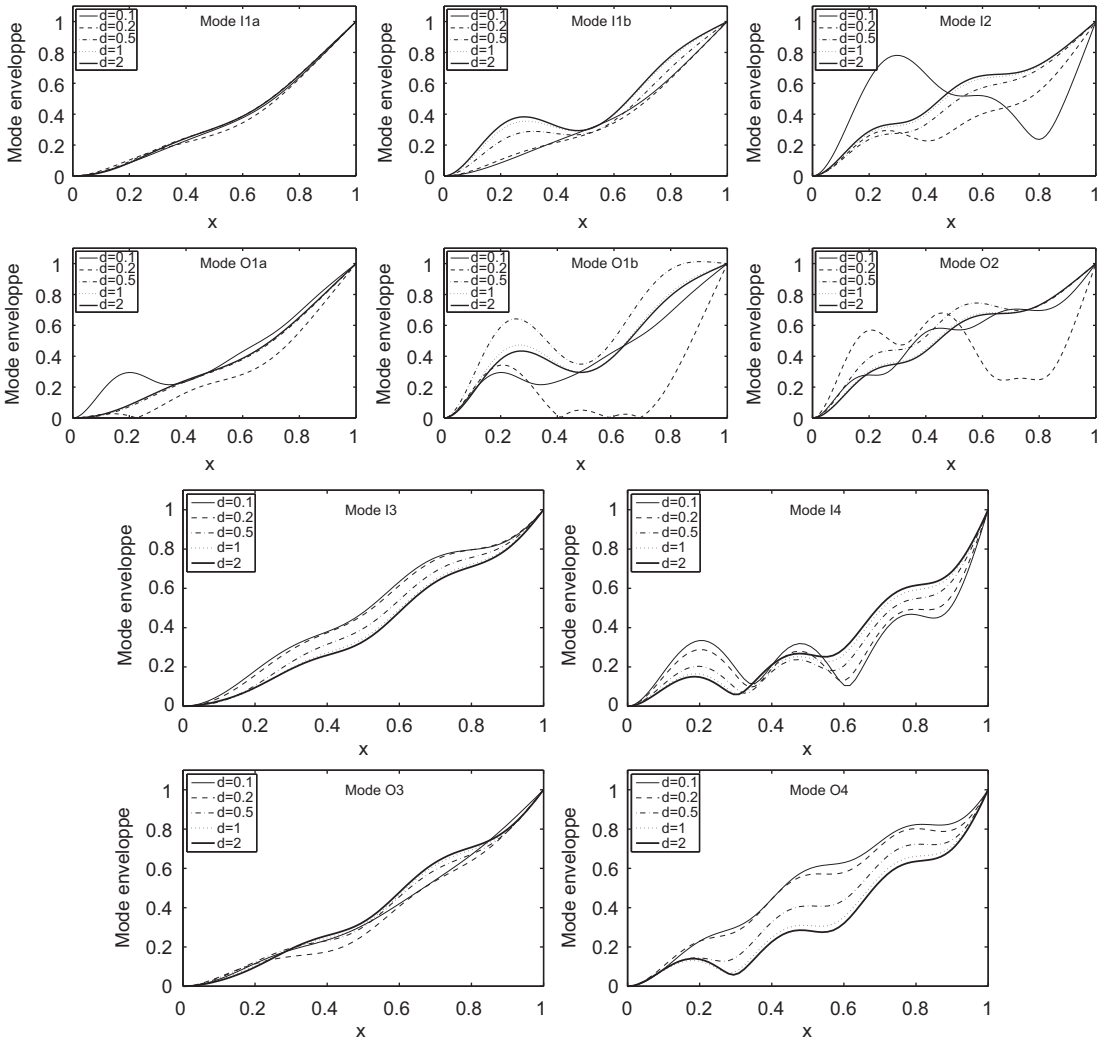

Fig. 10. Evolution with d of the envelope of the least stable in-phase and out-of-phase modes for $M^* = 4$ and $U^* = 13$. The indexing of the modes corresponds to Fig. 8. The envelope is computed as the maximum vertical deflection achieved for $0 \leq x \leq 1$, for one of the two flags after normalizing the mode amplitude so that the amplitude at the trailing edge is always unity.

This frequency jump and its variability with the parameter values are clearly visible in Fig. 6. The frequency plots show some large variations of the dominant frequency with M^* and U^* for given d. Large frequency values can be achieved at low U^* (for large value of the plates' rigidity). We must point out that these frequencies occur mostly in the stability region where all modes have negative growth rates. In some situations, large dominant frequencies can also occur for unstable configurations but at very small separation distance (typically less than 5% of the plates' length as seen for $M^* = 2$ in Fig. 6). In the presence of a small amount of material damping or flow viscosity (neglected here), we expect these high-frequency modes to be the most affected.

4. Stability of three coupled plates

In the case of three evenly spaced identical plates, three different types of modes are obtained that correspond to the mode types observed experimentally (see Fig. 1):

(i) an in-phase mode (I) where all three plates flap in phase; the correlation coefficients as defined in (33) satisfy $r_{12} = r_{13} = r_{23} = 1$ and the outer plates have the same motion;

(ii) an out-of-phase mode (O) where the outer plates flap in phase with the same amplitude and the middle plate flaps with a phase equal to π with respect to the other plates ($r_{12} = r_{23} = -1$ and $r_{13} = 1$);
(iii) a symmetric mode (S) where the outer plates have opposite vertical displacements and the middle plate remains still: $r_{13} = -1$ and $\zeta^{(2)}(x) = 0$.

A symmetry argument for the existence of mode (S) will be given in Section 5. The same symmetry argument will also prove that plates 1 and 3 always have equal or opposite motions, therefore their relative motion amplitude is equal to 1. However, in modes I and O, the motion of the center plate is in general not of the same amplitude as the two others' (although it was observed that it had the same x dependence leading to a correlation coefficient of ± 1).

For a given value of M^*, Fig. 11 shows the evolution of the mode properties in the (d, U^*)-plane. We observe that at short distances and for light plates (large M^*), the dominant mode structure is highly sensitive to the problem parameters, with the presence of finger-shaped regions of dominance of the (O) and (S) modes. At large distances the out-of-phase mode (O) prevails as for two plates. However for large d, the modes group in triplets. Within each triplet,

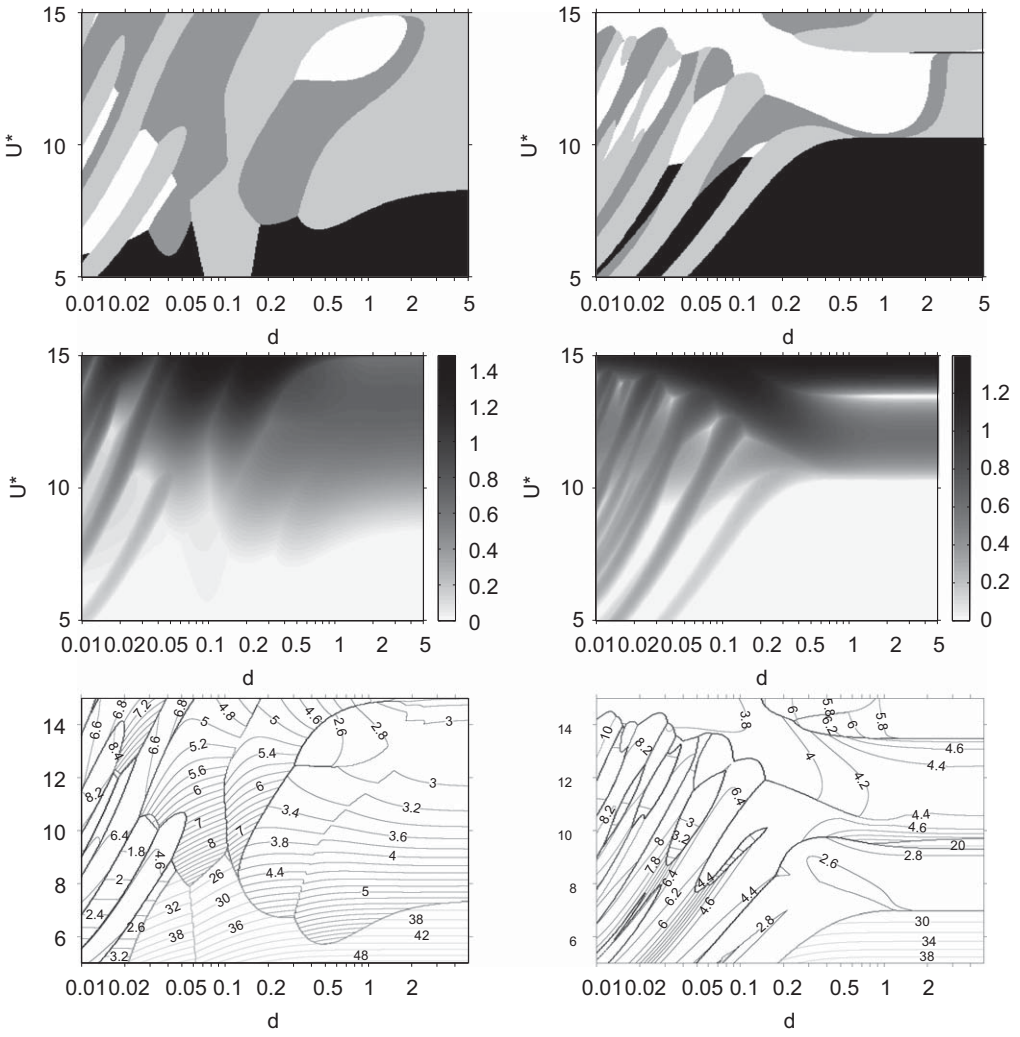

Fig. 11. Evolution of the dominant mode properties for three plates with $M^* = 3$ (left) and $M^* = 10$ (right). (Top) The nature of the dominant mode is given in the (d, U^*)-plane: stability region (black), symmetric mode S (dark gray), out-of-phase mode O (light gray) and in-phase mode I (white). (Center) The maximum growth rate is plotted in the (d, U^*)-plane. Stability regions correspond to a zero growth rate for clarity. (Bottom) Contours of the dominant mode's frequency in the (d, U^*)-plane.

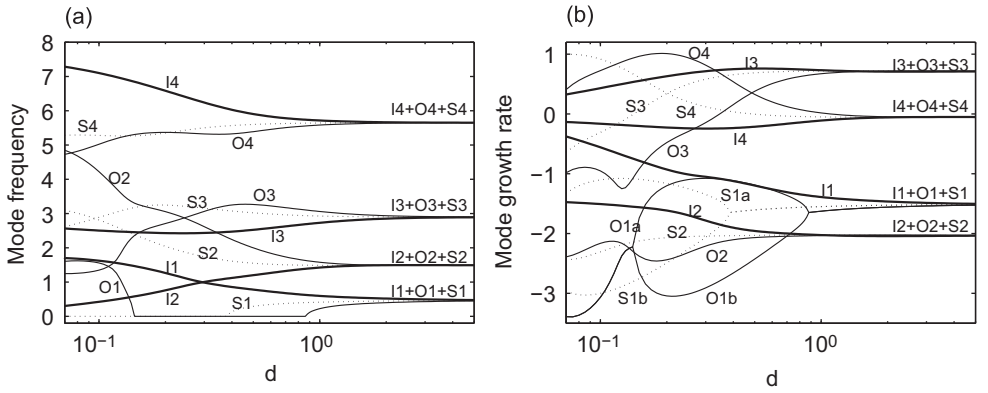

Fig. 12. Evolution of the frequency (left) and growth rate (right) of the first four in-phase, out-of phase and symmetric modes for three plates with $M^* = 3$ and $U^* = 13$. The branches corresponding to in-phase, out-of-phase and symmetric modes are plotted respectively with thick solid lines, thin solid lines and dotted lines.

one finds a mode of each kind (I, O and S) with frequency, growth rate and envelope asymptotically equal to the values for one plate only (Fig. 12). For the particular choice $M^* = 3$ and $U^* = 13$, we observe that for increasing d, the dominant mode takes alternatively each of the three possible natures (Fig. 12). As for two plates, a switch in the dominant mode can lead to a sudden change of all the following: mode nature (I,O,S), mode structure and frequency.

5. Results for larger N

5.1. Symmetry argument

In the previous sections, we have observed that all the modes are always symmetric or antisymmetric in structure with respect to the axis of symmetry (between the two plates for $N = 2$ or on the middle plate for $N = 3$). We attempt here to provide a physical argument for this observation. A mathematical proof involving the structure of the matrices in (30) is presented in Appendix B.

The orientation of the horizontal axis is physically determined by the forcing flow. The orientation of the vertical axis is however purely arbitrary. For a particular mode, define $\zeta^{(j)}(x)$ the displacement of the plate clamped at $y = (j-1)d$. Defining a new y-coordinate y' as $y' = (N-1)d - y$ and a new indexing of the plates $j' = N+1-j$ will leave the problem absolutely unchanged. In this new situation, the displacement of the plate sitting at $y' = (j-1)d$ in a particular mode will be $-\zeta^{(N+1-j)}(x)$. However, the physical problem is unchanged and the mode itself cannot have been modified, therefore there must exist a constant λ such that

$$\zeta^{(j)}(x) = -\lambda\zeta^{(N+1-j)}(x) \quad \text{for all } 1 \le j \le N. \tag{34}$$

Considering the previous equality for any pair $j = p$ and $j = N+1-p$ ($1 \le p \le N$), we see that $\lambda = \pm 1$. In a particular mode, the displacements of plates j and $N+1-j$ must therefore be equal or opposite.

The correlation coefficient of the two plates as defined in (33) must be equal to ± 1. Therefore, *the motion of the N plates must be symmetric or antisymmetric with respect to the plane located between plates $N/2$ and $N/2+1$ (resp. on plate $(N+1)/2$) for even N (resp. odd N).*

One consequence of this result is that for odd values of N, symmetric modes correspond to a center plate at rest, as was observed for the case of three plates in Section 4.

5.2. The limit $N \to \infty$

We now consider the limit case of a large number of plates N. This geometry is particularly relevant in the study of plate assemblies as found in cooling systems or in some nuclear reactors (Miller, 1960; Kim and Davis, 1995; Guo and Païdoussis, 2000a). Since the problem is invariant by a translation of d along the vertical axis, we look for solutions of

(7) in which the displacement $\zeta^{(n)}$ and pressure perturbation $[p]^{(n)}$ of plate n ($-\infty<n<\infty$) are of the form

$$\zeta^{(n)}(x)=\zeta^{(0)}(x)\mathrm{e}^{\mathrm{i}n\varphi},\quad [p]^{(n)}(x)=[p]^{(0)}(x)\mathrm{e}^{\mathrm{i}n\varphi} \tag{35}$$

with the phase φ being arbitrary between 0 and 2π. From (20), we obtain $[p]^{(0)}$ from $\zeta^{(0)}$ as

$$\frac{1}{2\pi}\int_0^1 K_\infty(x-\xi,\varphi)[p]'^{(0)}(\xi)\,\mathrm{d}\xi=-\omega^2\zeta^{(0)}+2\mathrm{i}\omega\frac{\mathrm{d}\zeta^{(0)}}{\mathrm{d}x}+\frac{\mathrm{d}^2\zeta^{(0)}}{\mathrm{d}x^2},\quad \int_0^1 [p]'^{(0)}(\xi)\,\mathrm{d}\xi=0 \tag{36}$$

with the modified kernel K_∞ given by

$$K_\infty(u,\varphi)=\frac{1}{u}+2\sum_{n=1}^{\infty}\frac{u\cos n\varphi}{u^2+n^2d^2}. \tag{37}$$

We note here that K_∞ is an even function of φ (as expected since the problem is invariant by reversing the labeling order of the plates). In the following, we therefore restrict our study to $0\le\varphi\le\pi$. Using Fourier series, we can determine K_∞ explicitly as

$$K_\infty(u,\varphi)=\frac{\pi}{d}\frac{\cosh\left[\frac{u}{d}(\pi-\varphi)\right]}{\sinh\left(\frac{\pi u}{d}\right)}\quad \text{for } 0\le\varphi\le\pi. \tag{38}$$

The case $\varphi=0$ will correspond to a purely in-phase mode (all the plates will have the same motion) and the case $\varphi=\pi$ corresponds to the purely out-of-phase mode (any two consecutive plates have opposite vertical displacements). Guo and Païdoussis (2000a) studied the latter mode exclusively by assuming the symmetry property to simplify the potential flow problem. They also used a different geometry with free boundary conditions applied at the leading and trailing edges, the side edges of the plate being clamped to a rigid wall. Here, we do not assume *a priori* a particular phase difference φ but instead consider all possible values of φ to determine the most unstable mode and its nature.

5.2.1. Stability threshold at large N

For a given φ, we can use the same approach as in Section 2 and decompose $\zeta^{(0)}$ over the first Q fundamental modes of the clamped–free beam. For each mode $\zeta_m^{(0)}$, we then obtain from (36) and (21) the pressure gradients $[p^{(M)}]_m'^{(0)}$, $[p^{(G)}]_m'^{(0)}$ and $[p^{(K)}]_m'^{(0)}$. For each value of φ, we compute the critical stability curve in the (M^*, U^*) plane of the modes with a phase difference φ between successive plates, and obtain the absolute stability curve by taking the intersection of the stability domains. The results are shown in Fig. 13 for two values of the relative distance of the plates $d=0.2$ and 0.5, and compared to the results obtained using the method of Section 2 with an increasing number of plates. We observe that the results obtained for increasing values of N converge well to this limit boundary as $N\to\infty$. We also observe that the stability curve converges rather fast toward this limit for both values of d. Most of the limit stability curve is obtained with a very good approximation for $N\ge 5$.

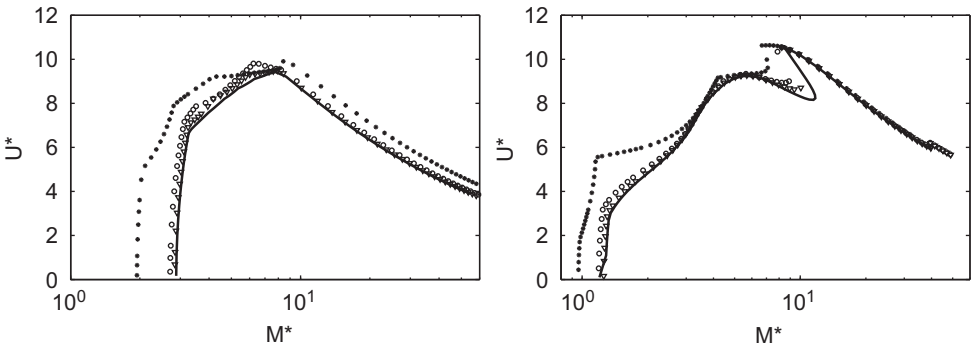

Fig. 13. Evolution of the critical stability curve in the (M^*, U^*)-plane for $d=0.2$ (left) and $d=0.5$ (right), and an increasing number of plates: $N=2$ (stars), $N=5$ (circles) and $N=10$ (triangles). The limit $N\to\infty$ described in Section 5.2 is plotted as a thick black line.

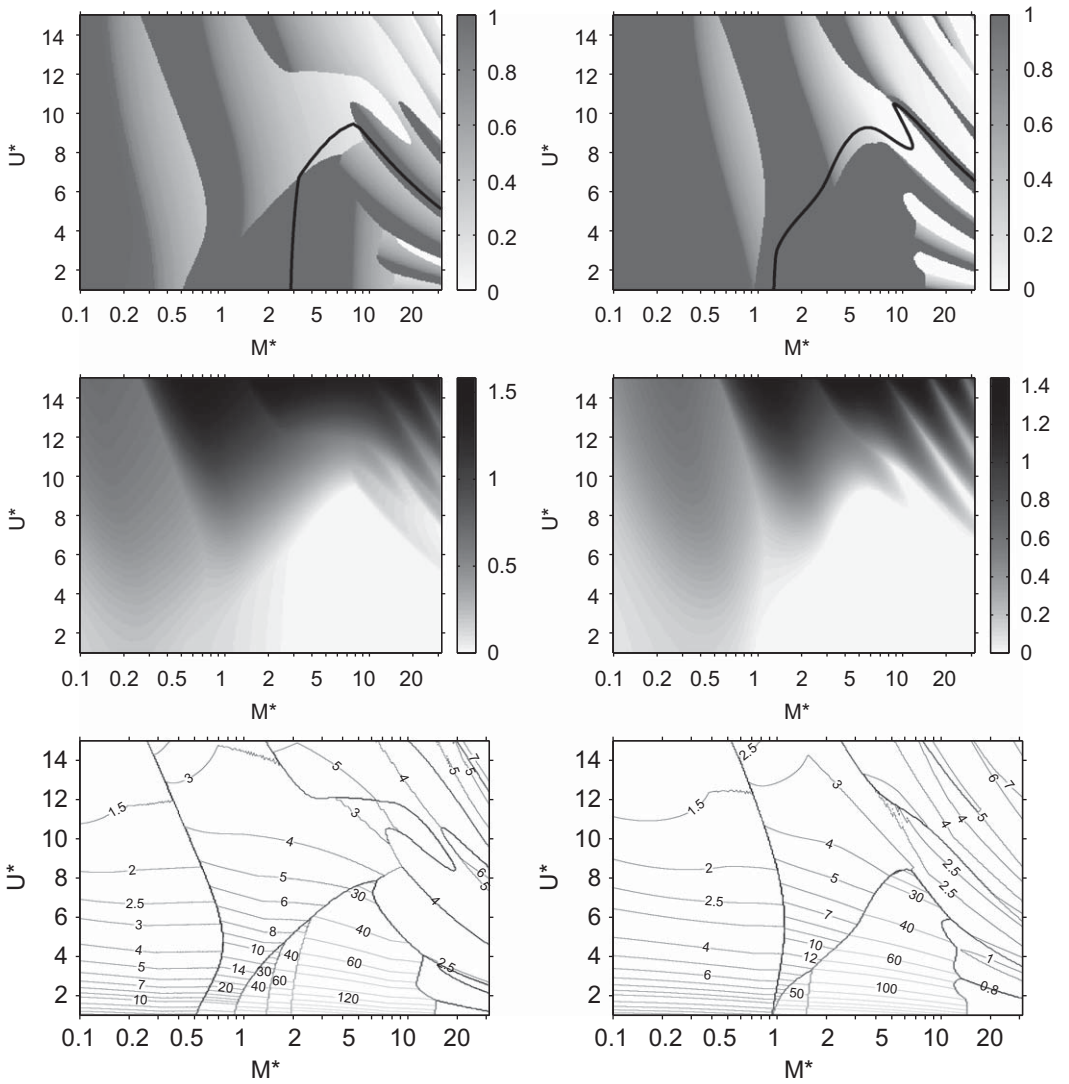

Fig. 14. Evolution in the (M^*, U^*)-plane of the properties of the dominant mode for an infinite number of equally spaced plates positioned at a distance $d = 0.2$ (left) and $d = 0.5$ (right) from each other. (Top) Relative phase φ between two consecutive plates (normalized by π). $\varphi/\pi = 1$ correspond to the purely out-of-phase mode where one plate's motion is opposite to its two neighbors. $\varphi/\pi = 0$ corresponds to the in-phase mode where all plates flap in phase. For reference, the stability curve of Fig. 13 is also plotted (thick black line). (Center) Growth rate of the dominant mode. (Bottom) Frequency of the dominant mode.

5.2.2. *Properties of the dominant mode in the $N \to \infty$ limit*

Using the same method, we can compute the frequency and growth rate of the modes with a phase difference equal to φ. For a given value of M^*, U^* and d, we search over all the possible values of φ for the most unstable mode. The properties of the dominant mode are shown in Fig. 14: the phase difference between two consecutive plates in that mode, as well as this mode's frequency and growth rate, are successively studied. While the out-of-phase mode ($\varphi = \pi$) tends to dominate for lower values of M^* and larger values of d, it is not necessarily the case. In particular, for large values of M^* or small values of d, the in-phase mode can be dominant. We also note that the transition from $\varphi = 0$ to $\varphi = \pi$ in the dominant mode is not necessarily discontinuous but that dominant modes with any value of φ can be found for a particular value of M^*, U^* or d. This seems to contradict the assumption of Guo and Païdoussis (2000a) that the out-of-phase mode is dominant in the linear regime. We must, however, point out that Guo and Païdoussis (2000a) considered free–free boundary conditions, while the present work considers clamped–free plates. The change in

boundary conditions is expected to have a significant impact on the position of the critical stability curve in the (M^*, U^*)-plane (Guo and Païdoussis, 2000b).

We noted previously that the convergence of the stability curve with increasing N is a rather fast but inhomogeneous process; some parts of the curve are obtained with a very good approximation for N as low 4 or 5, while others require a larger number of plates (Fig. 13). From the top panel of Fig. 14, we observe that the zones of fast convergence correspond to regions of the parameter space where the purely out-of-phase mode is dominant ($\varphi = \pi$), while the slowest converging regions correspond to smaller values of φ. Physically, a mode with a phase difference φ between two successive plates can be seen as a wave traveling along the vertical axis with a wavelength equal to $2\pi d/\varphi$ and the number of plates necessary to describe that mode is of the order of $2\pi/\varphi$. For $\varphi \sim \pi$, the instability is well described by the motion of a plate coupled to its two nearest neighbors, while for small φ, a large number of plates is necessary to describe the structure of the mode accurately. The stability and properties of local modes (those described by a small number of plates) are less influenced by the total number of plates in the system.

6. Conclusions

Using the double-wake approach, we have performed the linear stability analysis of an array of N parallel and identical flexible plates clamped at their leading edge in a horizontal flow. The behavior of two and three plates was discussed in more detail, as well as the limit of an infinite number of plates.

This method allows one to reproduce important properties of the coupled motion of two plates observed in numerical and experimental studies. For a finite relative distance d between the plates, two types of modes are observed, corresponding to in-phase or out-of-phase motions of the plates. The linear stability framework allows one to obtain a map of the dominant modes in the (M^*, U^*, d)-space, and we observed that, while it is possible to observe a transition from in-phase to out-of-phase for increasing d and a particular choice of (M^*, U^*), in some situations the in-phase or the out-of-phase modes are dominant for all d, consistent with some recent experiments (Jia et al., 2007). In general, the presence of a second plate was shown to destabilize the straight rest position. The destabilizing effect was observed to be most significant for heavy or short flags (small M^*). This preferential destabilization for small M^* was also observed in Guo and Païdoussis (2000b) for the stability of a single plate in a channel, linking this destabilization to confinement effects. Our analysis also shows that the dominant mode properties are strongly influenced by the fluid–solid inertia ratio M^*: the out-of-phase mode is linearly dominant for all values of d for heavy plates (small M^*), as observed numerically by Tang and Païdoussis (2009), while the in-phase mode can be dominant for larger values of M^*.

In the case of $N = 3$ plates, three types of modes (symmetric, in-phase and out-of-phase) were observed, consistently with recent wind-tunnel experiments by Schouveiler and Eloy. The case of an infinite number of plates was then discussed. The stability curve was obtained as well as the properties of the most unstable mode. The out-of-phase mode (with two consecutive plates having opposite displacements) was shown to be the most unstable for low M^* and larger values of d. However, modes with any value of the phase difference $\varphi \in [0, \pi]$ were shown to exist for some parameter values. The phase difference of the most unstable mode (or equivalently the number of plates necessary to describe this mode) was observed to condition the convergence of the stability curve for increasing N.

The advantage of the present approach over the one-dimensional approach developed in Jia et al. (2007) and Shelley et al. (2005) lies in its ability to take into account the finite length of the plate and the presence of a wake enforcing a trailing edge regularity condition. However, additional modeling work is needed to include a more accurate representation of the vortical wake. From the comparison between the present double-wake approach and the vortex sheet representation for one plate, we expect the former to behave relatively well for larger values of M^*. For shorter or heavier flags, the influence of the wake is expected to be more important and we anticipate some discrepancies.

Acknowledgment

This work was supported by the Human Frontier Science Program Research Grant RGY 0073/2005.

Appendix A. Numerical solution of a singular Cauchy-like integral equation

We are interested here in the numerical solution of a integral equations for $\kappa_1(x)$ and $\kappa_2(x)$ of the form

$$\frac{1}{2\pi}\int_0^1 \frac{\kappa_1(x')\,\mathrm{d}x'}{x - x'} + \int_0^1 K(x, x')\kappa_2(x')\,\mathrm{d}x' = f_1(x), \tag{39a}$$

$$\int_0^1 K(x,x')\kappa_1(x')\,\mathrm{d}x' + \frac{1}{2\pi}\int_0^1 \frac{\kappa_2(x')\,\mathrm{d}x'}{x-x'} = f_2(x), \tag{39b}$$

$$\int_0^1 \kappa_1(x')\,\mathrm{d}x' = \int_0^1 \kappa_2(x')\,\mathrm{d}x' = 0, \tag{39c}$$

where the kernel $K(x,x')$ is regular for $1 \le \{x,x'\} \le 1$. Eq. (39c) is necessary for the system to be well-posed because of the Cauchy nature of the kernels involved in the integral equation (Tuck, 1980).

Following Tuck (1980), both integral equations are then integrated in x

$$\frac{1}{2\pi}\int_0^1 \kappa_1(x')\log|x-x'|\,\mathrm{d}x' + \int_0^1 L(x,x')\kappa_2(x')\,\mathrm{d}x' = g_1(x) + \gamma_1, \tag{40a}$$

$$\int_0^1 L(x,x')\kappa_1(x')\,\mathrm{d}x' + \frac{1}{2\pi}\int_0^1 \kappa_2(x')\log|x-x'|\,\mathrm{d}x' = g_2(x) + \gamma_2, \tag{40b}$$

where $K(x,x') = \partial L/\partial x$ and $f_j(x) = g_j'(x)$, and γ_j are unknown constants. Because of the logarithmic nature of the kernel, we expect κ_j to have square-root singularities at both ends of the interval of integration. We therefore define the regularized functions $\tilde{\kappa}_j(x) = \kappa_j(x)\sqrt{x(1-x)}$.

Take N_p Gauss–Chebyshev points defined as

$$x_p = \frac{1-\cos\theta_p}{2}, \quad \theta_p = \frac{(p-\frac{1}{2})\pi}{N_p}, \quad 1 \le p \le N_p. \tag{41}$$

We denote by $\tilde{\boldsymbol{\kappa}}_{\boldsymbol{j}}$ the vector of the values of $\tilde{\kappa}_j(x_p)$. Using the change of variables $x' = (1-\cos\theta')/2$ in (40) leads to (remembering that $\int_0^1 \kappa_j(x')\,\mathrm{d}x' = \int_0^\pi \tilde{\kappa}_j(\theta')\,\mathrm{d}\theta' = 0$)

$$\frac{1}{2\pi}\int_0^\pi \tilde{\kappa}_1(\theta')\log|2x-(1-\cos\theta')|\,\mathrm{d}\theta' + \int_0^\pi L(x,\theta')\tilde{\kappa}_2(\theta')\,\mathrm{d}\theta' = g_1(x) + \gamma_1, \tag{42a}$$

$$\int_0^\pi L(x,\theta')\tilde{\kappa}_1(\theta')\,\mathrm{d}\theta' + \frac{1}{2\pi}\int_0^\pi \tilde{\kappa}_2(\theta')\log|2x-(1-\cos\theta')|\,\mathrm{d}\theta' = g_2(x) + \gamma_2, \tag{42b}$$

where for convenience of notation we understand $\tilde{\kappa}(\theta')$ to mean $\tilde{\kappa}(x(\theta'))$. The previous system is then evaluated at $x = x_p$ and the different integrals in θ' are divided into N_p intervals of equal length centered on θ_p. For example, for the regular kernel L,

$$\int_0^\pi L(x_p,\theta')\tilde{\kappa}_j(\theta')\,\mathrm{d}\theta' = \sum_{n=1}^{N_p}\int_{\theta_n^c}^{\theta_{n+1}^c} L(x_p,\theta')\tilde{\kappa}_j(\theta')\,\mathrm{d}\theta' \sim \sum_{n=1}^{N_p}\tilde{\kappa}_j(\theta_n)\int_{\theta_n^c}^{\theta_{n+1}^c} L(x_p,\theta')\,\mathrm{d}\theta' \tag{43}$$

with $\theta_n^c = (n-1)\pi/N_p$ for $1 \le n \le N_p+1$, and therefore $\theta_p = (\theta_p^c + \theta_{p+1}^c)/2$. The evaluation of the integral involving the logarithmic kernel is more subtle. The integral can still be split over the N_p equal intervals, and evaluated as previously for $n \ne p$. We evaluate separately the case $n = p$. Using the definition of x_p in terms of θ_p:

$$\int_{\theta_p^c}^{\theta_{p+1}^c} \tilde{\kappa}_j(\theta')\log\left|2x_p-(1-\cos\theta')\right|\mathrm{d}\theta' = \int_{\theta_p^c}^{\theta_{p+1}^c} \tilde{\kappa}_j(\theta')\log\left|\cos\theta'-\cos\theta_p\right|\mathrm{d}\theta'. \tag{44}$$

On this interval, $|\theta'-\theta_p| \le \Delta\theta/2$ with $\Delta\theta = \pi/N_p$. Assuming this interval is small, we can expand $\tilde{\kappa}(\theta')$ and $\cos\theta' - \cos\theta_p$ about θ_p. Keeping only the dominant terms in $\Delta\theta$, we obtain

$$\int_{\theta_p^c}^{\theta_{p+1}^c} \tilde{\kappa}_j(\theta')\log\left|2x_p-(1-\cos\theta')\right|\mathrm{d}\theta' \sim \tilde{\kappa}_j(\theta_p)\Delta\theta\left(\log\left|\frac{\sin\theta_p\,\Delta\theta}{2}\right| - 1\right). \tag{45}$$

Using these results, Eq. (40) is approximated as

$$\mathbf{C}\cdot\begin{pmatrix}\tilde{\boldsymbol{\kappa}}_1\\ \tilde{\boldsymbol{\kappa}}_2\end{pmatrix} = \begin{pmatrix}\mathbf{C^{(1)}} & \mathbf{C^{(2)}}\\ \mathbf{C^{(2)}} & \mathbf{C^{(1)}}\end{pmatrix}\cdot\begin{pmatrix}\tilde{\boldsymbol{\kappa}}_1\\ \tilde{\boldsymbol{\kappa}}_2\end{pmatrix} = \begin{pmatrix}\mathbf{g_1}\\ \mathbf{g_2}\end{pmatrix} + \gamma_1\begin{pmatrix}\mathbf{1}\\ \mathbf{0}\end{pmatrix} + \gamma_2\begin{pmatrix}\mathbf{0}\\ \mathbf{1}\end{pmatrix} \tag{46}$$

with $\mathbf{1}$ and $\mathbf{0}$ the column vectors of N_p elements all equal respectively to 1 and 0. The influence coefficient matrices $\mathbf{C^{(1)}}$ and $\mathbf{C^{(2)}}$ have coefficients

$$C_{mn}^{(1)} = \frac{1}{2\pi}\int_{\theta_n^c}^{\theta_{n+1}^c} \log|2x_m - 1 + \cos\theta'|\,\mathrm{d}x', \quad C_{mn}^{(2)} = \int_{\theta_n^c}^{\theta_{n+1}^c} L(x_m,\theta')\,\mathrm{d}\theta'. \tag{47}$$

All the terms of $\mathbf{C}^{(2)}$ and the nondiagonal terms of $\mathbf{C}^{(1)}$ are obtained using the trapezoidal rule. Diagonal terms of $\mathbf{C}^{(1)}$ are obtained using (45). The integration in x to obtain L and g_j is done using a Gauss–Chebyshev quadrature [see for example Pozrikidis (1998)].

The matrix $\mathbf{C}$ is nonsingular and can be inverted:

$$\begin{pmatrix} \tilde{\boldsymbol{\kappa}}_1 \\ \tilde{\boldsymbol{\kappa}}_2 \end{pmatrix} = \mathbf{C}^{-1}.\left[\begin{pmatrix} \mathbf{g}_1 \\ \mathbf{g}_2 \end{pmatrix} + \gamma_1 \begin{pmatrix} \mathbf{1} \\ \mathbf{0} \end{pmatrix} + \gamma_2 \begin{pmatrix} \mathbf{0} \\ \mathbf{1} \end{pmatrix}\right], \tag{48}$$

and the constants γ_1 and γ_2 are obtained by enforcing $\int_0^\pi \tilde{\kappa}_j(\theta')\,\mathrm{d}\theta' = 0$. Note that the case $\int_0^1 \kappa_i(x)\,\mathrm{d}x = \alpha_i$ with α_i a nonzero (known) constant is handled just as easily using this method. The approach is also easily transposed to the case of N functions κ_j as in (20).

Appendix B. Symmetry of the modes

We provide here a more rigorous mathematical argument for the symmetry or antisymmetry of all the modes with respect to the middle plane (understood as the plane $y = (N-1)d/2$). For N plates, the problem is doubly symmetric in the following sense: the effect of an arbitrary displacement, velocity or acceleration of plate i on the pressure jump on plate j is exactly equal to the effect of *the same* arbitrary displacement, velocity or acceleration of plate j on the pressure jump on plate i, and is also equal to the effect of *the same* displacement, velocity or acceleration of plate $N+1-i$ on the pressure forcing on plate $N+1-j$. Mathematically, this is expressed by the symmetry and structure of the operator acting on the vector $([p]^{(1)}, [p]^{(2)}, \ldots, [p]^{(N)})$ in Eq. (20). If we rewrite Eq. (20) as

$$\mathscr{P}.\begin{pmatrix} [p]^{(1)} \\ \vdots \\ [p]^{(N)} \end{pmatrix} = \cdots \quad \text{with } \mathscr{P}_{ij}(f)(x) = \frac{1}{2\pi}\int_0^1 \frac{(x-\xi)f(\xi)\,\mathrm{d}\xi}{(x-\xi)^2 + (i-j)^2 d^2}, \tag{49}$$

then the operator matrix $\mathscr{P}$ is such that $\mathscr{P}_{ij}$ only depends on $|i-j|$. Then one can prove easily that its inverse $\mathscr{Q}$ satisfies

$$\mathscr{Q}_{ij} = \mathscr{Q}_{N-i,N-j}. \tag{50}$$

A close look at the definition of the five different matrices defined in (30) will show that they satisfy the same symmetry *by block*, and we explain here what we mean by that. Let $\mathbf{B}$ be the matrix in bracket in (30), and define the block matrices $\tilde{\boldsymbol{B}}^{(\boldsymbol{ij})}$ with $1 \le \{i,j\} \le N$ such that $B_{(i-1)Q+q,(j-1)Q+s} = \tilde{B}^{(ij)}_{qs}$ for $1 \le \{q,s\} \le Q$, then

$$\tilde{\boldsymbol{B}}^{(\boldsymbol{ij})} = \tilde{\boldsymbol{B}}^{(\boldsymbol{N+1-j,N+1-i})}. \tag{51}$$

Decomposing in the same way the eigenvector $\boldsymbol{\alpha}$ in blocks $\tilde{\boldsymbol{\alpha}}$: $\alpha_{(j-1)Q+s} = \tilde{\alpha}^{(j)}_s$, Eq. (30) becomes

$$\sum_{j=1}^{N}\sum_{s=1}^{Q} \tilde{B}^{(ij)}_{qs}\tilde{\alpha}^{(j)}_s = 0, \tag{52}$$

for $1 \le i \le N$ and $1 \le q \le Q$. But, through (51) we also have

$$\sum_{j=1}^{N}\sum_{s=1}^{Q} \tilde{B}^{(ij)}_{qs}\tilde{\alpha}^{(N+1-j)}_s = \sum_{j'=1}^{N}\sum_{s=1}^{Q} \tilde{B}^{(i,N+1-j')}_{qs}\tilde{\alpha}^{(j')}_s = \sum_{j'=1}^{N}\sum_{s=1}^{Q} \tilde{B}^{(N+1-i,j')}_{qs}\tilde{\alpha}^{(j')}_s = 0, \tag{53}$$

for $1 \le i \le N$ and $1 \le q \le Q$. The vector $\boldsymbol{\beta}$ defined as $\beta_{(j-1)Q+s} = \tilde{\alpha}^{(N+1-j)}_s$ is also an eigenvector of $\mathbf{B}$. It is therefore proportional to $\boldsymbol{\alpha}$ and

$$\tilde{\alpha}^{(j)}_s = \lambda\tilde{\alpha}^{(N+1-j)}_s \quad \text{for } 1 \le j \le N \text{ and } 1 \le s \le Q. \tag{54}$$

Applying this relationship twice, we find immediately that $\lambda^2 = 1$ and $\lambda = \pm 1$. $\boldsymbol{\alpha}$ gives the decomposition of the eigenmode along the basis built from the free modes. This symmetry property therefore immediately transfers to the displacement of the plates in a particular mode $\zeta^{(j)}_m(x)$ with $1 \le j \le N$ and $1 \le m \le N \times Q$:

$$\zeta^{(j)}_m(x) = \pm\zeta^{(N+1-j)}_m(x). \tag{55}$$

References

Argentina, M., Mahadevan, L., 2005. Fluid-flow-induced flutter of a flag. Proceeding of the National Academy of Science 102, 1829–1834.

Balint, T.S., Lucey, A.D., 2005. Instability of a cantilevered flexible plate in viscous channel flow. Journal of Fluids and Structures 20, 893–912.

Bisplinghoff, R.L., Ashley, H., Halfman, R.L., 1955. Aeroelasticity. Addison-Wesley, Reading, MA.

Connell, B.S.H., Yue, D.K.P., 2007. Flapping dynamics of a flag in uniform stream. Journal of Fluid Mechanics 581, 33–67.

Eloy, C., Lagrange, R., Souilliez, C., Schouveiler, L., 2008. Aeroelastic instability of a flexible plate in a uniform flow. Journal of Fluid Mechanics 611, 97–106.

Eloy, C., Souilliez, C., Schouveiler, L., 2007. Flutter of a rectangular plate. Journal of Fluids and Structures 23, 904–919.

Farnell, D.J.J., David, T., Barton, D.C., 2004. Coupled states of flapping flags. Journal of Fluids and Structures 19, 29–36.

Guo, C.Q., Païdoussis, M.P., 2000a. Analysis of hydroelastic instabilities of rectangular parallel-plate assemblies. ASME Journal of Pressure Vessel Technology 122, 502–508.

Guo, C.Q., Païdoussis, M.P., 2000b. Stability of rectangular plates with free side-edges in two-dimensional inviscid channel flow. Journal of Applied Mechanics 67, 171–176.

Huang, L., 1995. Flutter of cantilevered plates in axial flow. Journal of Fluids and Structures 9, 127–147.

Huang, W.-X., Shin, S.J., Sung, H.J., 2007. Simulation of flexible filaments in uniform flow by the immersed boundary method. Journal of Computational Physics 226, 2206–2228.

Jia, L.-B., Li, F., Yin, X.-Z., Yin, X.-Y., 2007. Coupling modes between two flapping filaments. Journal of Fluid Mechanics 581, 199–220.

Kim, G., Davis, D.C., 1995. Hydrodynamic instabilities in flat-plate-type fuel assemblies. Nuclear Engineering and Design 158, 1–17.

Kornecki, A., Dowell, E.H., O'Brien, J., 1976. On the aeroelastic instability of two-dimensional panels in uniform incompressible flow. Journal of Sound and Vibration 47, 163–178.

Lemaitre, C., Hémon, P., deLangre, E., 2005. Instability of a long ribbon hanging in axial air flow. Journal of Fluids and Structures 20, 913–925.

Michelin, S., Llewellyn Smith, S.G., Glover, B.J., 2008. Vortex shedding model of a flapping flag. Journal of Fluid Mechanics 617, 1–10.

Michelin, S., Llewellyn Smith, S.G., 2009. Falling cards and flapping flags: understanding fluid-solid interactions using an unsteady point vortex model. Theoretical and Computational Fluid Dynamics, in press.

Miller, D.R., 1960. Critical flow velocities for collapse of reactor parallel-plate fuel assemblies. ASME, Journal of Engineering for Power 82, 83–95.

Païdoussis, M.P., 1998. Fluid–Structure Interactions, Slender Structures and Axial Flows, vol. 1. Academic Press, London.

Païdoussis, M.P., 2004. Fluid–Structure Interactions, Slender Structures and Axial Flows, vol. 2. Academic Press, London.

Pozrikidis, C., 1998. Numerical Computation in Science and Engineering. Oxford University Press, Oxford.

Shelley, M., Vandenberghe, N., Zhang, J., 2005. Heavy flags undergo spontaneous oscillations in flowing water. Physical Review Letters 94, 094302.

Tang, L., Païdoussis, M.P., 2009. The coupled dynamics of two cantilevered flexible plates in axial flow. Journal of Sound and Vibration 323, 214–231.

Theodorsen, T., 1935. General theory of aerodynamic instability and the mechanism of flutter. NACA Report 496.

Tuck, E.O., 1980. Application and solution of Cauchy singular integral equations. In: Anderssen, R.S.F.R.d.H., Lukas, M.A. (Eds.), The Application and Numerical Solution of Integral Equations. Sijthoof and Noordhoff, Alphen aan den Rijn, pp. 21–50.

Watanabe, Y., Suzuki, S., Sugihara, M., Sueoka, Y., 2002. An experimental study of paper flutter. Journal of Fluids and Structures 16, 529–542.

Zhang, J., Childress, S., Libchaber, A., Shelley, M., 2000. Flexible filaments in a flowing soap film as a model for one-dimensional flags in a two-dimensional wind. Nature 408, 835–839.

Zhu, L., Peskin, C., 2002. Simulation of flapping flexible filament in a flowing soap film by the immersed boundary method. Journal of Computational Physics 179, 452–468.

Zhu, L., Peskin, C., 2003. Interaction of two flapping filaments in a flowing soap film. Physics of Fluids 15, 1954–1960.